Changes in Antarctic surface conditions and potential for ice shelf hydrofracturing from 1850 to 2200

Nicolas C. Jourdain[1], Charles Amory[2,1], Christoph Kittel[1], and Gaël Durand[1]

[1]Univ. Grenoble Alpes/CNRS/IRD/G-INP/INRAE, Institut des Geosciences de l'Environnement, Grenoble, France.
[2]Laboratoire des Sciences du Climat et de l'Environnement, LSCE/IPSL, CEA-CNRS-UVSQ, Université Paris-Saclay, 91191 Gif-sur-Yvette, France

Correspondence: Nicolas Jourdain (nicolas.jourdain@univ-grenoble-alpes.fr)

Abstract.

A mixed statistical-physical approach is used to emulate the spatio-temporal variability of the Antarctic Ice Sheet surface mass balance and surface melt rates of a regional climate model. We demonstrate the ability of this simple method to extend existing regional climate simulations to periods, scenarios or climate models, that were not originally simulated. This method is useful to quickly populate ensembles of surface mass balance and melt rates, which are needed to constrain ice sheet model ensembles. Here we apply this method to estimate: (i) the changes in Antarctic surface mass balance over 1850–2200 and the associated effect on sea level, and (ii) the changes in potential for ice shelf hydrofracturing.

After weighting 16 climate models to obtain a realistic distribution of the equilibrium climate sensitivity, we find a likely contribution of surface mass balance to sea level rise of -2.2 to -0.4 cm from 1900 to 2010, and -3.4 to -0.1 cm from 2000 to 2099 under the SSP1-2.6 scenario, versus -4.4 to -1.4 cm under SSP2-4.5, and -7.8 to -4.0 cm under SSP5-8.5. The contribution from 2000 to 2200 is highly uncertain: between -10 and -1 cm in SSP1-2.6 and between -33 and +6 cm in SSP5-8.5 depending on the climate model.

Based on a criterion on the presence of liquid water beyond firn saturation in our emulated ensemble, we estimate the surface conditions that make ice shelves prone to hydrofracturing. Our results suggest that a majority of Antarctic ice shelves could remain safe from hydrofracturing under the SSP1-2.6 scenario, but all of them could become prone to hydrofracturing before 2150 under the SSP5-8.5 scenario.

1 Introduction

In the 21st century, increasing snowfall over the Antarctic Ice Sheet is expected to compensate a significant part of the dynamical ice mass loss triggered by ocean warming, which mitigates the Antarctic contribution to sea level rise (e.g., Seroussi et al., 2020; Edwards et al., 2021; Fox-Kemper et al., 2021). However, models suggest that if air temperatures exceed ∼7.5°C above the 1981–2010 average, the increase in accumulation starts to be overwhelmed by the mass loss through surface meltwater runoff into the ocean (Kittel et al., 2021; Coulon et al., 2023).

Runoff is a negative contribution to the surface mass balance. It is produced if surface melt and/or rain rates are high enough to (i) percolate and bring the temperature of underlying snow and firn layers to the freezing point, (ii) saturate the pore space

in the snow and firn layers, which is sometimes referred to as firn air depletion (Pfeffer et al., 1991; Kuipers Munneke et al., 2014; Alley et al., 2018), and (*iii*) flow into the ocean. The liquid water beyond firn saturation, hereafter often referred to as "~~liquid water in excess~~excess liquid water", does not necessarily flow into the ocean, especially in the case of a relatively flat surface. ~~Liquid water in excess~~ excess liquid water can indeed alternatively form ponds or be transported horizontally within the firn or at the ice surface (Kingslake et al., 2017; Bell et al., 2018).

The presence of ~~liquid water in excess~~ excess liquid water can trigger ice shelf break-up through hydrofracturing: in favorable conditions of ice shelf stress, the weight of liquid water can destabilize a fracture and lead to its unstoppable propagation as long as liquid water keeps filling the fracture (Weertman, 1973; Lai et al., 2020). Stress variations associated with surface meltwater ponding and drainage, causing flexure and fracture, can amplify this mechanism and propagate its effects spatially (Banwell et al., 2013, 2019). An entire ice shelf break-up nonetheless likely requires large amounts of meltwater production all over its surface, as observed before the break-up of Larsen A in 1995 and Larsen B in 2002 (Skvarca et al., 2004; Scambos et al., 2003; van den Broeke, 2005; Sergienko and Macayeal, 2005; Robel and Banwell, 2019; Wille et al., 2022).

When occurring on ice shelf parts that buttress the upstream flow, hydrofracturing and the resulting ice shelf collapse may strongly enhance the contribution of upstream glaciers to sea level rise (Fürst et al., 2016; Sun et al., 2020; Seroussi et al., 2024). Gilbert and Kittel (2021) estimated that 34% of Antarctic ice shelf area could be vulnerable to hydrofracturing at 4°C of warming above pre-industrial levels. The exact warming level needed to trigger the widespread presence of liquid water on a given ice shelf depends on the amount of snowfall and on the snow/firn temperature and density (Donat-Magnin et al., 2021; van Wessem et al., 2023).

The contribution of ice sheets to changes in sea level are estimated through ice sheet simulations driven, among other things, by spatio-temporal variations in SMB, and sometimes by the dates of collapse for individual ice shelves. In the Ice Sheet Model Intercomparison Project for the 6th Climate Model Intercomparison Project (CMIP6, Eyring et al., 2016; ISMIP6, Nowicki et al., 2016), these conditions were directly calculated from the CMIP model outputs (Nowicki et al., 2020; Seroussi et al., 2024). Despite progress in their representation of the Antarctic climate (Dunmire et al., 2022), the CMIP models often have a coarse resolution and include a relatively poor representation of snow processes over ice sheets, in particular with regard to firn saturation by meltwater and subsequent ponding or runoff (Nowicki et al., 2020).

Regional Climate Models (RCMs) dedicated to polar regions and constrained by CMIP projections offer a good alternative to the direct use of CMIP models for the estimation of surface conditions (e.g., Kuipers Munneke et al., 2014; Kittel et al., 2021). Despite detailed snow physics, a major weakness of RCMs is nonetheless the associated requirement for additional skills and processing/computing time, which is why RCM outputs were not ready on time for ISMIP6-Antarctica (Nowicki et al., 2020; Seroussi et al., 2020). Because of these difficulties, only a limited number of RCM-based projections are usually produced, which is generally insufficient to sample the CMIP model diversity~~regarding their~~. This may affect the representation of the recent period (Barthel et al., 2020) and ~~their~~ the sensitivity to increasing anthropogenic emissions (e.g. Hausfather et al., 2022) in the small RCM ensemble.

Over the years, Antarctic Ice Sheet modellers have often scaled their best estimates of present-day accumulation to temperature anomalies from the CMIP models (e.g., based on the Clausius-Clapeyron relationship as in Gregory and Huybrechts,

2006), while Positive Degree Day models have sometimes been used to derive melt rates (e.g., Rodehacke et al., 2020; Zheng et al., 2023). The ~~later~~ latter are based on daily air temperatures projected by the CMIP models, and can be calibrated to match RCM projections (Coulon et al., 2023). Other methods are emerging, based on the emulation of more complex models like RCMs (van der Meer et al., 2023) or firn models (Dunmire et al., 2024). In this paper, we present and evaluate a novel statistical–physical method that emulates the spatio-temporal evolution of the surface mass balance (SMB) and surface melt rates of a regional climate model (section 2). This method is applied in section 3 to provide confidence intervals on the changes in SMB and the associated changes in sea level, and on the changes in production of ~~liquid water in excess~~ excess liquid water and the implications for ice shelf hydrofracturing.

2 Methods

2.1 Approach

Here we estimate both the SMB evolution over the grounded ice sheet, for its equivalent change in global sea level, and the evolution of the liquid water production beyond firn saturation, for its potential to induce hydrofracturing. We build an ensemble of estimates over Antarctica, for the 1850–2100 period, driven by 16 CMIP6 models and three SSP (Shared Socioeconomic Pathway O'Neill et al., 2014) scenarios (Tab. 1). A smaller ensemble covers the 1850–2200 period, driven by only 8 CMIP6 models (see stars in Tab. 1) and two SSP scenarios (SSP1-2.6 and SSP5-8.5).

Our approach is based on a limited number of RCM simulations covering 1980–2100 or 1980–2200 (subsection 2.2), and the full ensemble is populated from a statistical-physical emulation method (subsection 2.3). The emulation method can be used to extend a given RCM simulation in time, to produce data for a scenario that was not covered by the RCM, or to produce data for a CMIP model that was never used to force the RCM (Fig. 1). These approaches are first evaluated separately (sections 2.3.3 to 2.3.5), then they are combined ~~with each other~~ (section 2.4) to produce the ensemble projections described in section 3.

2.2 Regional climate model projections

We make use of the MAR-3.11 regional climate model (Gallée and Schayes, 1994; Gallée, 1995; Kittel et al., 2021, 2022), which parameterises multiple processes relevant for polar environments. In MAR, the atmosphere is coupled to a 30-layer model representing the first 20 m of snow/firn with refined resolution at the surface. The snow/firn model solves prognostic equations for temperature, mass, water content, and snow properties (dendricity, sphericity, and grain size). In the presence of surface melting or rainfall, liquid water percolates downward into the next firn layers with a water retention of 5% of the porosity in each successive layer. The firn layers are fully permeable until they reach a close-off density of 830 $\mathrm{kg\,m^{-3}}$. To account for possible cracks in ice lenses and moulins, the part of available water that is transmitted downward to the next layer decreases as a linear function of firn density, from 100% transmitted at the close-off density to zero at 900 $\mathrm{kg\,m^{-3}}$ and beyond. If liquid water is not able to percolate further down, it remains where it is. When the entire porosity space in the uppermost

Table 1. CMIP6 models used to drive MAR simulations or emulations until 2100 in section 3. ECS stands for Equilibrium Climate Sensitivity, and the indicated values are from Meehl et al. (2020), except for NorESM2-MM which is from Seland et al. (2020). Stars beside model names indicate that the CMIP6 simulations were extended to ~~2300~~ 2200 under the SSP1-2.6 and ~~SSP-5.85~~ SSP5-8.5 pathways. The entries for the three SSP pathways indicate whether it was derived from the actual MAR simulation driven by this CMIP model under this scenario ("MAR"), from a MAR simulation driven by this CMIP model but for a warmer scenario ("from SSP5-8.5", i.e. method described in section 2.3.4), or emulated from six MAR simulations driven by different CMIP models ("from 6 models", i.e. method described in section 2.3.5). The historical period was directly available from the five CMIP models for which at least ~~a~~ one MAR projection was available, and it was emulated from 6 models for the other CMIP models.

CMIP model	Member	Reference	ECS	weight	SSP1-2.6	SSP2-4.5	SSP5-8.5
ACCESS-CM2 ⋆	r1i1p1f1	Bi et al. (2020)	4.7°C	0.11	from 6 models	from 6 models	from 6 models
ACCESS-ESM1-5 ⋆	r1i1p1f1	Ziehn et al. (2020)	3.9°C	0.24	from 6 models	from 6 models	from 6 models
CanESM5 ⋆	r1i1p1f1	Swart et al. (2019)	5.6°C	0.03	from 6 models	from 6 models	from 6 models
CESM2	r11i1p1f1	Danabasoglu et al. (2020)	5.2°C	0.06	MAR	MAR	MAR
CESM2-WACCM ⋆	r1i1p1f1	Gettelman et al. (2019)	4.8°C	0.10	from 6 models	from 6 models	from 6 models
CNRM-CM6-1	r1i1p1f2	Voldoire et al. (2019)	4.8°C	0.10	from SSP5-8.5	from SSP5-8.5	MAR
CNRM-ESM2-1	r1i1p1f2	Séférian et al. (2019)	4.8°C	0.10	from 6 models	from 6 models	from 6 models
GFDL-CM4	r1i1p1f1	Held et al. (2019)	3.9°C	0.24	-	from 6 models	from 6 models
GFDL-ESM4	r1i1p1f1	Dunne et al. (2020)	2.6°C	0.47	from 6 models	from 6 models	from 6 models
GISS-E2-1-H ⋆	r1i1p1f2	Kelley et al. (2020)	3.1°C	0.41	from 6 models	from 6 models	from 6 models
INM-CM5-0	r1i1p1f1	Volodin et al. (2017)	1.9°C	0.18	from 6 models	from 6 models	from 6 models
IPSL-CM6A-LR ⋆	r1i1p1f1	Boucher et al. (2020)	4.6°C	0.12	from SSP5-8.5	from SSP5-8.5	MAR
MPI-ESM1-2-HR	r1i1p1f1	Müller et al. (2018)	3.0°C	0.43	MAR	MAR	MAR
MRI-ESM2-0 ⋆	r1i1p1f1	Yukimoto et al. (2019)	3.2°C	0.39	from 6 models	from 6 models	from 6 models
NorESM2-MM	r1i1p1f1	Seland et al. (2020)	2.5°C	0.47	from 6 models	from 6 models	from 6 models
UKESM1-0-LL ⋆	r1i1p1f2	Sellar et al. (2020)	5.3°C	0.05	MAR	MAR	MAR

snow/firn layer is filled with liquid water or if the uppermost snow/firn layer is denser than 900 $\mathrm{kg\,m^{-3}}$, any additional surface melt is considered as runoff and removed from the snow/firn model. There is no representation of ponds or horizontal routing.

The surface mass balance and melting conditions produced by MAR have been evaluated in comparison to observational products in several studies and a qualitative comparison to a satellite estimate of melt pond volume indicates that MAR is able to capture the main characteristics of the present-day surface conditions (Appendix A).

The MAR simulations were run at 35 km resolution, and the outputs were conservatively interpolated onto a 4 km stereographic grid, following the atmospheric forcing protocol in ISMIP6. Unless specified otherwise, we use these 4 km data, and all spatial integrals presented in this study were calculated by accounting for the stereographic scale factor. The ice mask and the surface elevation are based on Bedmap2 (Fretwell et al., 2013). The actual grounded ice sheet and ice shelf areas are 12.286 and 1.737 million $\mathrm{km^2}$, respectively.

Our MAR simulations cover 1980–2100 and are driven by two CMIP5 and five CMIP6 models under a number of scenarios, as listed in Tab. 2. The MAR–IPSL-CM6A-LR projection goes until 2200 following the extended SSP5-8.5 scenario (Shared Socioeconomic Pathways, Meinshausen et al., 2020). The selection of these specific CMIP models was based both on the availability of 6-hourly outputs (required to provide MAR boundary conditions), on the evaluation of their present-day mean characteristics (Agosta et al., 2019, 2024; Barthel et al., 2020), and on the diversity of their sensitivity to anthropogenic emissions. The latter is characterised by the Equilibrium Climate Sensitivity (ECS Hausfather et al., 2022), which is the increase in global mean surface air temperature that follows a doubling of atmospheric carbon dioxide.

For computational reasons, all simulation years were run in parallel with 20 years of spin-up to equilibrate the firn properties (e.g., 2051 is spun up from the transient 2031–2050 period). The initial state (e.g., 01-JAN-2031 for the simulation of 2051) is taken from the MAR–ACCESS-1.3 RCP8.5 simulation (Tab. 2), itself spun up from a previous version of MAR at 50 km resolution driven by NorESM1-M under RCP8.5 and spun up for 30 years from a present-day MAR simulation. A spin up of 20 years is generally sufficient to remove any sensitivity to the initial state (Donat-Magnin et al., 2021, their Fig. 12).

Table 2. List of CMIP models, their ensemble member number, their Equilibrium Climate Sensitivity (ECS, provided by Meehl et al., 2020), and the scenarios for which we have a MAR simulation driven by this CMIP model. The historical MAR simulations only start in 1980, and the projections go until 2100 unless specified otherwise. The model references are provided in Tab. 1.

CMIP model	era	member	ECS (°C)	Available MAR simulation
ACCESS-1.3	CMIP5	r1i1p1	3.5	historical, RCP8.5
NorESM1-M	CMIP5	r1i1p1	2.8	historical, RCP8.5
CESM2	CMIP6	r11i1p1f1	5.2	historical, SSP1-2.6, SSP2-4.5, SSP5-8.5
CNRM-CM6-1	CMIP6	r1i1p1f2	4.8	historical, SSP5-8.5
IPSL-CM6A-LR	CMIP6	r1i1p1f1	4.6	historical, SSP5-8.5 until 2200
MPI-ESM1-2-HR	CMIP6	r1i1p1f1	3.0	historical, SSP1-2.6, SSP2-4.5, SSP5-8.5
UKESM1-0-LL	CMIP6	r1i1p1f2	5.3	historical, SSP1-2.6, SSP2-4.5, SSP5-8.5

2.3 Statistical-physical emulation method

Hereafter, we first describe how the RCM projections of surface mass balance, surface melting and production of liquid water beyond firn saturation can be extended in time, and to other scenarios or CMIP models. Then, we evaluate these emulated projections in comparison to the actual RCM projections. In this subsection, we assume that runoff is equal to the production of liquid water beyond firn saturation as in the RCM, but we will use a different approach for the projections presented in section 3.

2.3.1 Rationale

Precipitation in Antarctica mostly consists of snowfall even in a warmer climate ~~(Kittel et al., 2021; Donat-Magnin et al., 2021)~~ (Kittel et al., 2021; Donat-Magnin et al., 2021, see also Appendix B). In first approximation, snowfall in Antarctica (SNF) thus

increases with air temperature following the Clausius-Clapeyron law, which can be approximated as:

$$\mathrm{SNF}(T_{\mathrm{ref}} + \Delta T) = \mathrm{SNF}(T_{\mathrm{ref}}) \times e^{a \Delta T} \tag{1}$$

where T_{ref} is a reference air temperature, ΔT the air warming, and a is typically 0.07 in polar conditions (Donat-Magnin et al., 2021).

Previous modelling studies also found an empirical exponential relationship between surface melt rate (MLT) and air warming:

$$\mathrm{MLT}(T_{\mathrm{ref}} + \Delta T) = \mathrm{MLT}(T_{\mathrm{ref}}) \times e^{b \Delta T} \tag{2}$$

where b is typically between 0.3 and 0.6 in Antarctica (Trusel et al., 2015; Donat-Magnin et al., 2021). In the following, we assume that ΔT is a variation in ~~near-surface~~ near-surface air temperature in both Eq. 1 and Eq. 2, which is a reasonable approximation given that the troposphere warms relatively uniformly from the surface to $\sim$300 hPa (Donat-Magnin et al., 2021, their Fig. 1).

Then, we introduce the r parameter, a threshold over which liquid water is produced beyond firn saturation, which occurs when the melt rate exceeds what can be stored and refrozen in the ongoing snow/firn accumulation (Pfeffer et al., 1991; Kuipers Munneke et al., 2014; Donat-Magnin et al., 2021; van Wessem et al., 2023), i.e., if:

$$\frac{\mathrm{MLT}}{\mathrm{SNF}} \geq r \tag{3}$$

where r is typically between 0.60 and 0.85 depending on the snow properties (Donat-Magnin et al., 2021). Here we do not attempt to ~~know~~ determine whether the excess of liquid water forms ponds or flows directly into the ocean (runoff), which is why the same r value will be used on the grounded ice sheet and on ice shelves. ~~The presence of rainfall makes~~

In Eq. 3~~more complex (see Appendix B of Donat-Magnin et al., 2021), but rainfallis generally negligible compared to snowfall in present-day conditions and to surface melt rates in much warmer conditions (Donat-Magnin et al., 2021). Furthermore, the only RCM simulation~~ , the effect of rainfall, sublimation and drifting-snow erosion are assumed to be negligible. Sublimation remains below 10% of snowfall even in a warmer climate (Kittel et al., 2021, their Tabs. S2-S3), and drifting-snow erosion is at least an order of magnitude smaller than sublimation (Gadde and van de Berg, 2024). As shown in Appendix B, rainfall represents less than 15% of the total precipitation on the grounded ice sheet until 2200 ~~(MAR–IPSL-CM6A-LR, SSP5-8.5) does simulate the actual rainfall/snowfall distribution and still has a positive surface mass balance over~~ and on the ice shelves ~~in 2200 (see section 3), which indicates that snowfall is still dominant over rainfall . In our method , we therefore assume that precipitation is entirely made of snow, and we neglect sublimation and drifting snow given their small contribution (Agosta et al., 2019)~~until 2100. The impact of neglecting rainfall in our method is discussed in Appendix B.

In this paper, we use these relationships to extrapolate SMB, melt rates, and the production of liquid water beyond firn saturation, to warmer or colder surface conditions. We assume that all the quantities at near-surface air temperature T_{ref} are perfectly known from the RCM, and we want to estimate them for a temperature change of ΔT that is provided by a CMIP model. To do so, we use the following sequence of equations, in which RU is the rate of mass loss through runoff (< 0), while

surface melt rate is defined positive:

$$\begin{cases} \mathrm{SNF}(T_{\mathrm{ref}}+\Delta T) &= (\mathrm{SMB}(T_{\mathrm{ref}})-\mathrm{RU}(T_{\mathrm{ref}}))\times e^{a\Delta T} \\ \mathrm{MLT}(T_{\mathrm{ref}}+\Delta T) &= min\{\mathrm{MLT}(T_{\mathrm{ref}})\times e^{b\Delta T}, m\} \\ \mathrm{RU}(T_{\mathrm{ref}}+\Delta T) &= -max\{0, \mathrm{MLT}(T_{\mathrm{ref}}+\Delta T) - r\,\mathrm{SNF}(T_{\mathrm{ref}}+\Delta T)\} \\ \mathrm{SMB}(T_{\mathrm{ref}}+\Delta T) &= \mathrm{SNF}(T_{\mathrm{ref}}+\Delta T)+\mathrm{RU}(T_{\mathrm{ref}}+\Delta T) \end{cases} \quad (4)$$

where a, b and m, and r are the method parameters. The m parameter is introduced to avoid unrealistically high melt rates. For the emulation, we assume that the emulated runoff (RU) is equal to the production rate of liquid water beyond firn saturation, as in the RCM.

In section 3, we emulate surface conditions for periods (Fig. 1a), scenarios (Fig. 1b), or CMIP models (Fig. 1c) that are not covered by existing MAR simulations. Our aim is to populate a large ensemble of surface conditions that can be used to drive ensembles of ice sheet and sea level projections, without the cost of running many RCM simulations and the associated need for 6-hourly outputs in the corresponding CMIP simulations. We first assess the performance of the emulation method for other periods, scenarios and CMIP models in subsections 2.3.3 to 2.3.5, then we combine them together in section 3 based on this assessment.

In this work, we use annual means for all the variables, which is consistent with usual datasets available for ice sheet models (e.g. Nowicki et al., 2020). To emulate a surface variable at a given warming or cooling level, we always calculate the emulation from 20 different years (i.e., different values of T_{ref} and ΔT), then we average the 20 emulated values (Fig. 1). This is done to better sample natural variability and to generate an emulated variability that is mostly related to the CMIP model temperatures. It also makes the emulation more robust from a statistical point of view.

2.3.2 Parameter calibration

The a and b parameters are obtained through a least-mean-square fitting of an exponential curve for SMB minus model runoff on the one hand, and for the surface melt rate on the other hand. Appendix C provides more details on the fitting method and gives the a and b values for individual models. On average, $a = 0.068$ and $b = 0.320$.

The maximum local melt rate (m parameter in Eq. 4) is set to the 99.99$^{\mathrm{th}}$ percentile of 1980-2100 local melt rates ($m = 1.80\times10^{-4}\ \mathrm{kg\,m^{-2}\,s^{-1}}$, i.e., 15.5 $\mathrm{mm\,day^{-1}}$). The value of r is more difficult to calibrate as it depends on the density and temperature of snow and on the threshold used to consider that liquid water is produced beyond firn saturation (Pfeffer et al., 1991; Donat-Magnin et al., 2021), so we will assess values in the 0.50–0.90 range, which includes the values used in previous work.

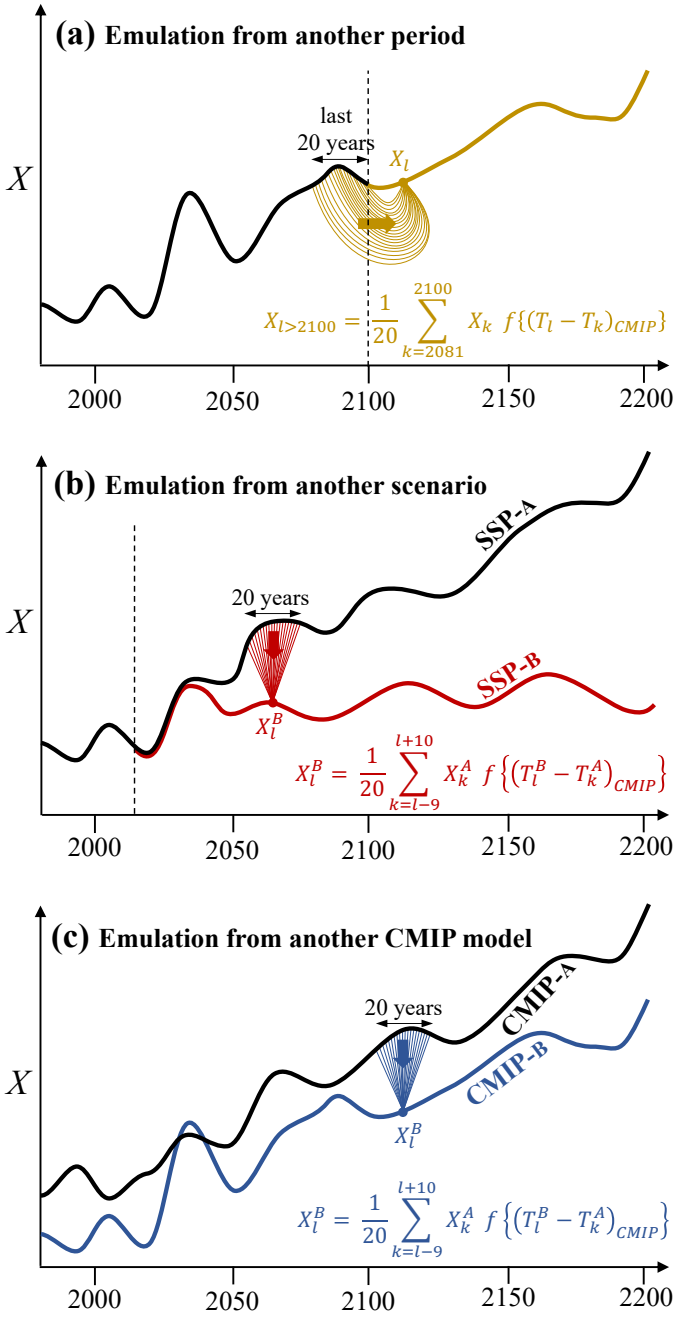

Figure 1. Schematic of the application of our emulation methodology (Eq. 4) to (a) extend the data to periods ~~non~~ not simulated by MAR (subsection 2.3.3), (b) extend the data to scenarios ~~non~~ not simulated by MAR (subsection 2.3.4), (c) extend the data to CMIP models ~~non~~ not downscaled by MAR (subsection 2.3.5). Variable X represents either or the surface melt rate. Function f represents one of the functions of ΔT provided in Eq. 4.

2.3.3 Emulation from another period

We first assess the ability of our emulation method (Eq. 4) to extend a RCM simulation backward or forward in time, based on the air temperatures of the corresponding CMIP model over the extended periods (Fig. 1a). The benefits of this method would be to extend 1980–2100 RCM simulations to 1850–2200.

For the evaluation, we emulate backward and forward in time from the 2081-2100 period of MAR–IPSL-CM6A-LR–SSP5-8.5, and we compare the emulated fields to the original MAR simulation (Fig. 2). In the original MAR simulation, the grounded ice sheet SMB increases linearly until ∼2100 due to increasing snowfall, then decreases when surface melt and resulting runoff become important (black lines in Fig. 2a,c,e). Over the ice shelves, the SMB in the original MAR simulation remains steady until ∼2090 then drops due to increased runoff, with ~~a~~ an SMB in 2200 that is 2000 $\mathrm{Gt\,yr^{-1}}$ lower than in 1995–2014 (black lines in Fig. 2b,d,f).

The emulation backward to pre-2081, i.e., towards a colder climate, is less biased than the emulation forward to post-2100, i.e., towards a warmer climate (Fig. 2). Over the grounded ice sheet, the forward-emulated SMB has biases that remain small over the first 10 years, and reasonable (∼10%) over the first 20 years for $r = 0.5$ and $r = 0.6$. However, the forward emulation fails to represent SMB after 2120 due to a significantly underestimated runoff. This is largely due to the inability of our emulation method to initiate melting at locations that never experienced melting over 2081–2100. The backward emulation over the grounded ice sheet is quite accurate for the first 20 years, i.e. for moderate changes in climate conditions, and is moderately low-biased back to 2015.

Over the ice shelves, the emulation forward is accurate in the first 50 years (Fig. 2b,d,f). The best results over this first period are obtained for $r = 0.50$ and $r = 0.60$. After 2150, melt rates in the original MAR simulation start increasing more linearly with time and our emulation overestimates melt rates and therefore mass loss. This is likely due to feedbacks that are represented in the MAR simulations but not in the IPSL-CM6A-LR model or in our emulation method. Indeed, the appearance of bare ice and changes in the cloud radiative properties have a strong impact on the projected SMB over Greenland (Hofer et al., 2020; Mostue et al., 2023), and a similar effect could be found in warmer conditions in Antarctica (Kittel et al., 2022). For a CMIP model like IPSL-CM6A-LR that fails to represent melt water runoff, our emulation method towards a warmer climate is nonetheless preferable to directly estimating the SMB from the CMIP model outputs (see black dashed lines in Fig. 2a,b).

From this first evaluation, we conclude that our emulation method is suitable for the extension of RCM simulations into a warmer future, for a maximum of 20 years over the grounded ice sheet and 50 years over the ice shelves. The extension to colder conditions in the past is more accurate as our emulation method is more suitable for reducing melt rates than for creating new melting areas. In the following, we use $r = 0.60$ as it fits well the original simulation while remaining within the range of previous studies. The spatial patterns are also well represented by this method (Appendix D, Fig. D1).

2.3.4 Emulation from another scenario

We now assess the ability of our method to emulate several scenarios from a MAR simulation driven by a warmer scenario (Fig. 1b). As mentioned previously, our method is not able to create new melting areas, but it is well suited to decrease melt

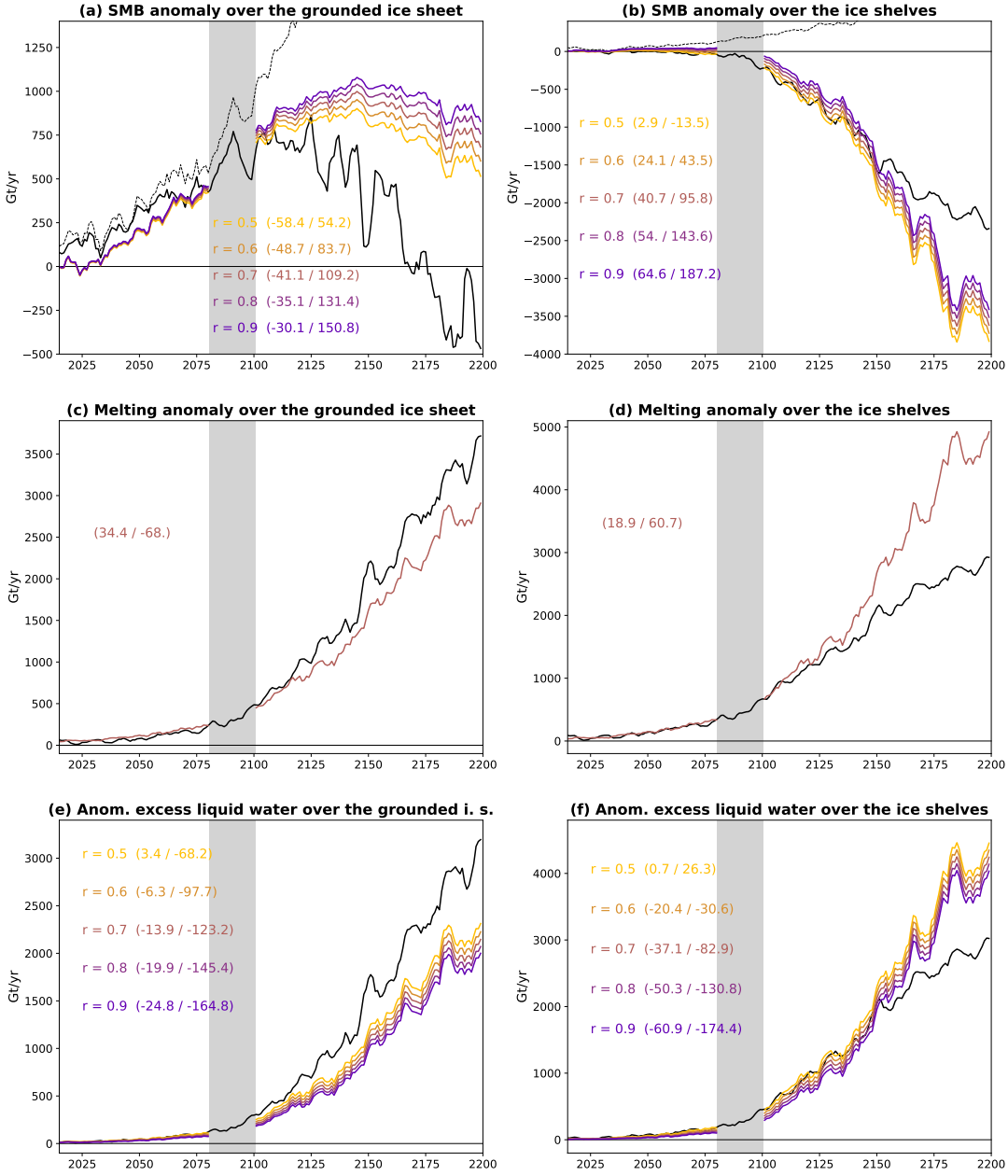

Figure 2. Evaluation of the emulation from another period (Fig. 1a) over the grounded ice sheet (left) and over the ice shelves (right), for SMB (upper), surface melting (middle) and the production of liquid water beyond firn saturation (lower). The solid black lines show the original MAR–IPSL-CM6A-LR simulation. The colored lines are the emulations from the 2081–2100 period (shaded in grey), both backward in time (left side of the grey area) or forward in time (right side of the grey area). The emulation is shown for several values of r (see Eq. 4) and the bias values are indicated for both 2061–2080 (20-year backward emulation) and 2101–2120 (20-year forward emulation). The black dashed lines in panels (a,b) show the SMB directly calculated from the IPSL-CM6A-LR outputs following the ISMIP6 approach (Nowicki et al., 2020, their Appendix C). The anomalies are calculated with respect to the 1995–2014 mean. The time series on this plot are filtered through a 5-year running average.

rates in colder conditions. We therefore consider the three MAR simulations for which we have the SSP1-2.6, SSP2-4.5 and SSP5-8.5 scenarios (MAR–CESM2, MAR–UKESM1-0-LL, MAR–MPI-ESM1-2-HR), and we evaluate the emulation of both SSP1-2.6 and SSP2-4.5 from SSP5-8.5. The calculations are done separately for each of the corresponding simulations (based on the parameters in Tab. C1), but the results are presented in Fig. 3 as averages over the three CMIP models.

Similarly as in the previous subsection, each emulated year is the average of 20 emulations from a reference ranging from 10 years before to 9 years after the emulated year (Fig. 1b). Doing so, the interannual variability of the extended variables is only attributed to the air temperature variability in the corresponding scenario.

The SSP1-2.6 and SSP2-4.5 emulated fields are quite accurate over the grounded ice sheet during the 21st century~~, even if the production of liquid water in excess is significantly underestimated in the last decades (~~: the biases indicated in Fig. 3 ~~a,c,e). Over the ice shelves, the emulated SSP1-2.6 SMB and runoff are close to the original simulations, but the emulated SSP2-4.5 runoff is underestimated and the SMB does not drop~~ for the emulated values are relatively low compared to the mean values simulated by MAR. The bias in emulated runoff becomes larger at the end of the 21st century ~~as in the original simulations~~ in the SSP2-4.5 scenario (Fig. 3~~b,d,f). From this evaluation,~~ e-f). This bias has little impact on the grounded ice sheet SMB (Fig. 3a) but cancels the small negative SMB anomaly simulated over the ice shelves near 2100 (Fig. 3b). These biases are small and limited to the end of the 21st century, so we conclude that our method is suitable for the emulation of multiple SSP scenarios based on an existing MAR simulation in a warmer scenario (here SSP5-8.5). The spatial patterns are also well represented by this method (Appendix D, Fig. D2).

2.3.5 Emulation from other CMIP models

Here we assess the ability of our method to emulate MAR simulations driven by other CMIP models (Fig. 1c). We consider five MAR simulations driven by different CMIP models under either SSP5-8.5 or RCP8.5, which have a similar radiative forcing. We assess the emulation from the same simulation (for verification of our method) and from six MAR simulations driven by other CMIP models. We use a similar methodology as in the previous subsection, calculating the average emulation of every year from 20 reference years (Fig. 1c), but instead of using the actual temperature as in the two previous subsections, we use the temperature anomaly with respect to each model's climatology. This was needed given that typical values of ~~surface~~ near-surface air temperature may vary from one CMIP model to another, in particular due to differences in the first level height and in their ability to represent stable surface boundary layers over ice sheets.

The method is evaluated in Fig. 4. First of all, ~~it is verified that~~ the minimal differences between the black dots on each radial and the coloured dot corresponding to the same climate model show that the biases are small for MAR simulations derived from themselves~~(Fig. 4), showing~~ . This shows that our methodology and its implementation are robust. We nonetheless note larger differences between the black dots on each radial and the coloured dots corresponding to the other climate models in Fig. 4c,d, indicating significant biases in melt rates when a MAR simulation is derived from another one~~, exceeding 100% in some cases (Fig. 4c,d), which~~ . This alters the emulated SMB (Fig. 4a,b). MAR–ACCESS1.3 is an outlier and leads to melt emulation with largest biases for the four other models. The realistic SMB emulations derived from MAR–ACCESS1.3 are mostly compensations between overestimated melt (Fig. 4c,d) and overestimated accumulation. The other CMIP5 simulation,

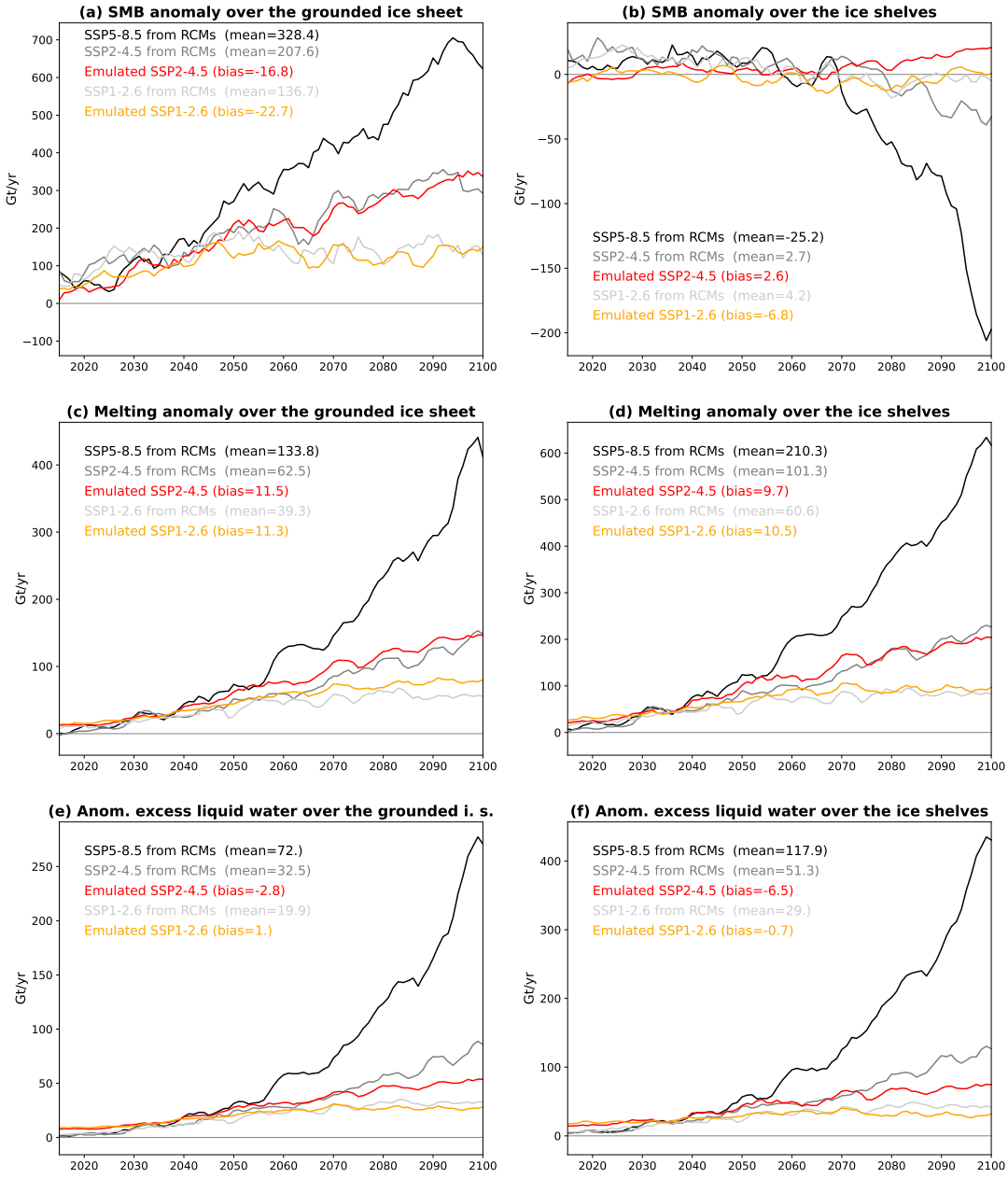

Figure 3. Evaluation of the emulation from a warmer scenario (Fig. 1b) over the grounded ice sheet (left) and over the ice shelves (right), for SMB (upper), surface melting (middle) and the production of liquid water beyond firn saturation (lower). The black and grey lines show the original MAR simulations, while the colored lines correspond to the emulated SSP1-2.6 and SSP2-4.5 scenarios based on the SSP5-8.5 MAR simulation and the CMIP ~~surface~~ near-surface air temperatures. Every line on this plot is the average of three simulations or emulations: MAR–CESM2, MAR–UKESM1-0-LL, MAR–MPI-ESM1-2-HR. The anomalies are calculated with respect to the 1995–2014 mean. The time series are filtered through a 5-year running average. The mean and biases over 2015–2100 are indicated on each panel.

MAR–NorESM1-M, is closer to the CMIP6 simulations even if the SMB is generally overestimated over the grounded ice sheet. The CMIP5 models have a relatively low ECS, and starting from MAR forced by any of these CMIP5 models does not give good emulations of models like CESM2 or CNRM-CM6-1 that both experience particularly strong warming over the 21st century (Kittel et al., 2021, 2022).

Given the biases of the emulation from a single model, we now assess the average of five emulations from different MAR simulations (excluding the simulation itself and the MAR–ACCESS1.3 outlier). The emulation is made for three SSP scenarios, based on the five MAR simulations under the same scenario if available or SSP5-8.5 otherwise. For clarity, we present the average results for MAR–CESM2, MAR–UKESM1-0-LL and MAR–MPI-ESM1-2-HR, which are the three MAR simulations for which we have all three scenarios (Fig. 5).

Averaging the emulation from several MAR simulations clearly improves the results, and the emulated SMB is generally quite accurate throughout the 21st century (Fig. 5a,b), although the mass loss at the surface of ice shelves is overestimated under SSP5-8.5 due to overestimated melt and runoff (Fig. 5d,f). Decreasing the r value would reduce the runoff bias here, but ~~possibly not for physical reasons, and not in the previous subsections~~changing the r value would neither be consistent with the results of the previous sections, nor reflect physical processes.

From this evaluation, we conclude that our multi-model emulation method is suitable for the emulation of MAR simulations driven by CMIP models that have never actually been used to drive MAR simulations. The spatial patterns are also well represented by this method (Appendix D, Fig. D3). It is important to stress that this method only gives meaningful results because of the average over several CMIP models, possibly due to the various responses of clouds and snow albedo from one model to another for a given warming level (Kittel et al., 2022).

2.4 Method used to build the ensemble of projections

Here we explain how we combine the three types of emulations summarized in Fig. 1 and how we weight the CMIP models to build our ensemble of projections. Then we explain how the liquid water beyond firn saturation is used in the SMB calculation and to estimate the potential for ice shelf hydrofracturing.

First, when the SSP5-8.5 MAR simulation driven by a given CMIP model is available but not the other scenarios, we emulate the SSP2-4.5 and SSP1-2.6 scenarios from SSP5-8.5 (blue curve in Fig. 6a). If MAR has not been driven at all by a given CMIP model, we emulate all scenarios from six MAR simulations driven by six CMIP models, taking the closest available scenario of a given model if several are available (see 1980–2100 in Fig. 6b). We then emulate the historical period from 1850 to 1979 for all models based on the 1980–1999 period which is the earliest period covered by the MAR simulations (gray curves in Fig. 6). For this, we use the method for emulating from another period (Fig. 1a).

For the projections between 2101 and 2200, we have a single MAR simulation forced by IPSL-CM6A-LR under SSP5-8.5 due to the non availability of 6-hourly 3-dimensional atmospheric data beyond 2100 for most CMIP models. The CMIP ~~surface~~ near-surface air temperatures are nonetheless available until 2200 for seven other simulations, for both the SSP1-2.6 and ~~SSP-5.85~~ SSP5-8.5 pathways (see stars in Tab. 1). For these seven simulations, we emulate the 22nd century based on the CMIP model temperatures and the MAR–IPSL-CM6A-LR simulation (see 2121–2200 in Fig. 6b). To ensure some continuity

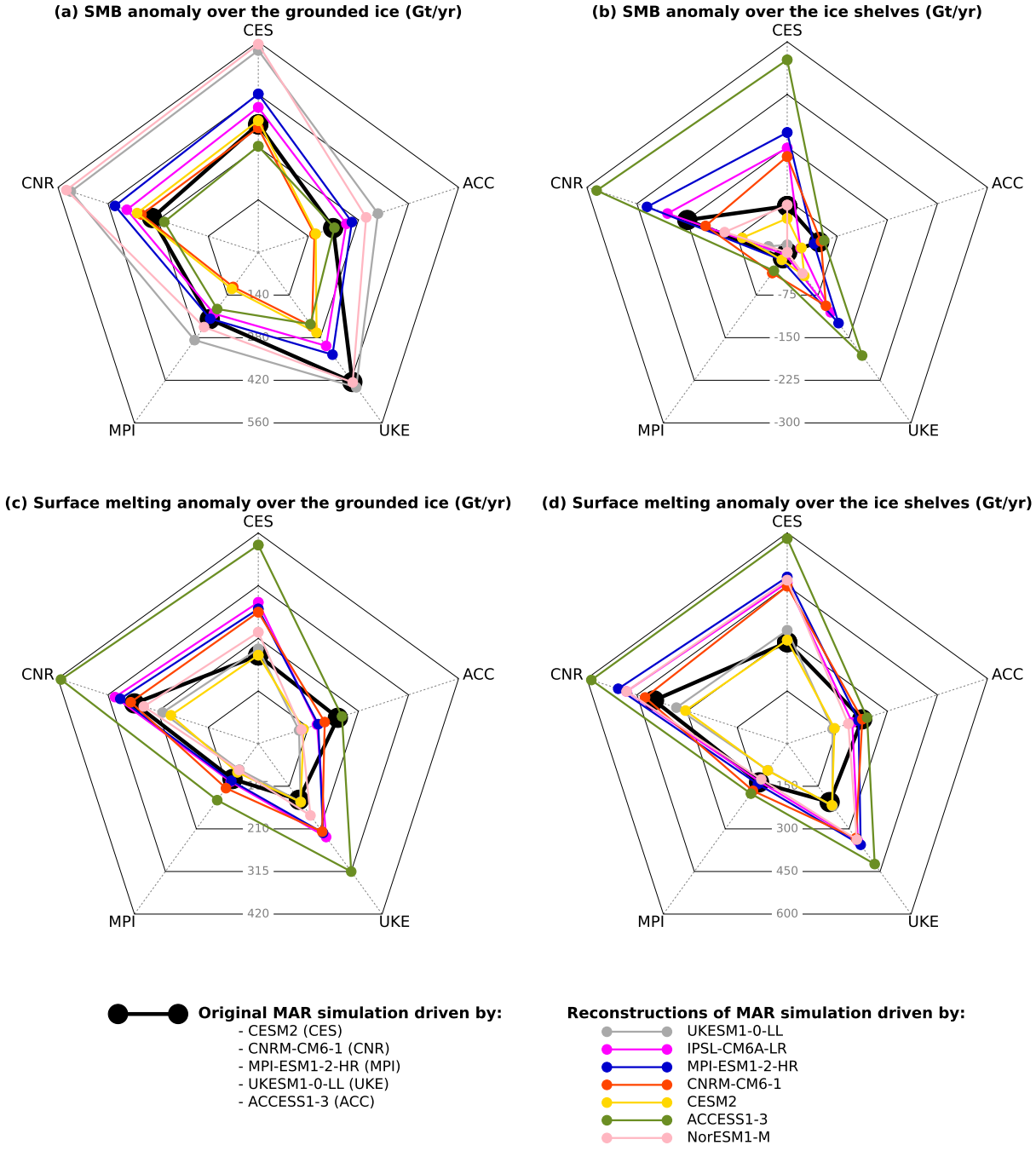

Figure 4. Evaluation of the emulation from other CMIP models (Fig. 1c) for SMB (upper panels) and surface melting (lower panels). The five radial lines correspond to five original MAR simulations driven by different CMIP6 or CMIP5 models, with the radial distance (thick black dots) indicating the SMB or melt rate values. The colored dots correspond to the emulated values from surface temperatures of another CMIP model. The black and colored pentagons link the dots for a better overview. The thin grey pentagons indicate the SMB or melt rate iso-value. The anomalies are calculated over 2015–2100 with respect to 1995–2014 under the SSP5-8.5 or RCP8.5 scenarios.

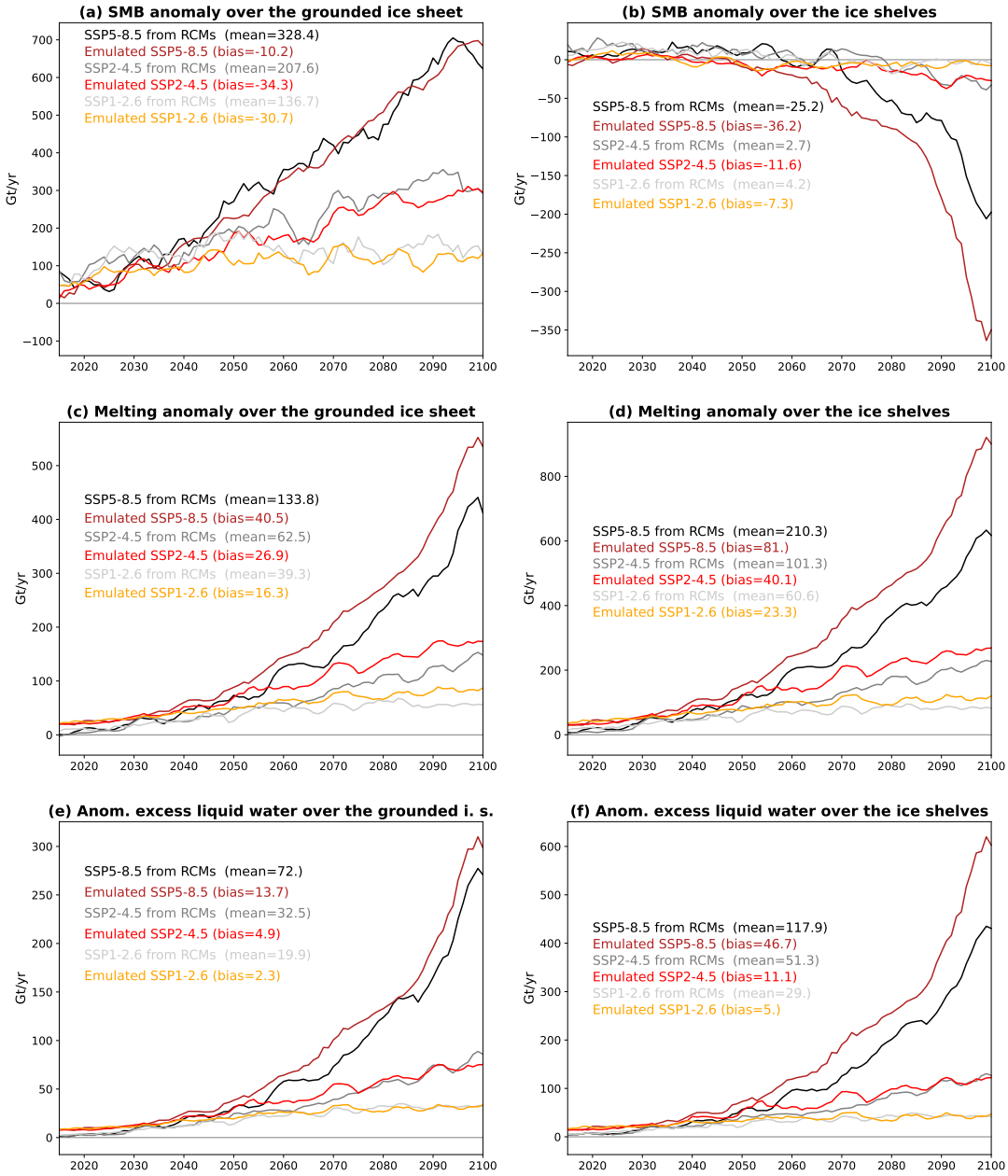

Figure 5. Evaluation of the emulation from five other CMIP models (Fig. 1c) over the grounded ice sheet (left) and over the ice shelves (right), for SMB (upper), surface melting (middle) and the production of liquid water beyond firn saturation (lower). The black and grey lines show the original MAR simulations for three SSP scenarios, while the colored lines correspond to the emulation of these simulations from 5 independent models. Every line on this plot is the average of three simulations or emulations: MAR–CESM2, MAR–UKESM1-0-LL, MAR–MPI-ESM1-2-HR. The anomalies are calculated with respect to the 1995–2014 mean. The time series are filtered through a 5-year running average. The mean and biases over 2015-2100 are indicated on each panel.

around 2100 and to benefit from better emulations before 2100, we apply a 20-year ramping transition (yellow area in Fig. 6b), over which we use a linear combination of the emulation from the 2081–2100 period and the emulation from MAR–IPSL-CM6A-LR. For the emulation of MAR–UKESM1-0-LL after 2100, we use the ensemble member r4i1p1f2 instead of r1i1p1f2 in the actual MAR simulations, because this is the only one available beyond 2100.

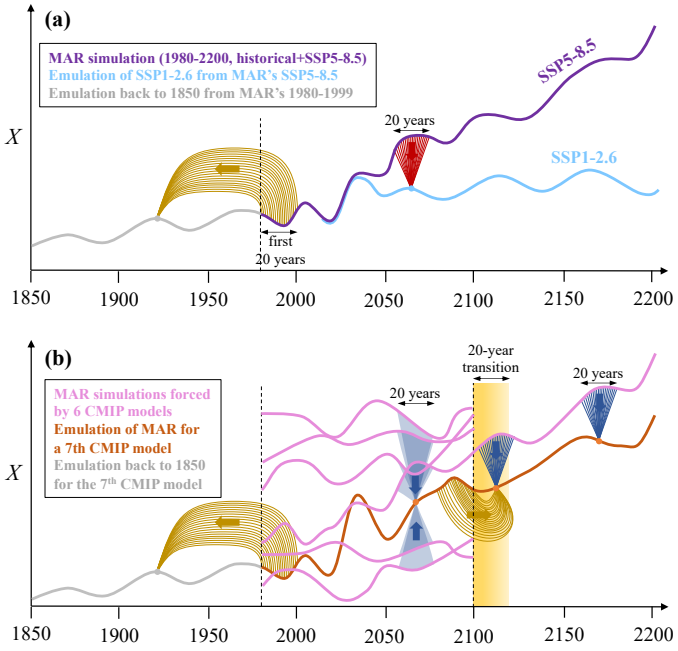

Figure 6. Schematic of the methods used to build our ensemble of projections. (a) a MAR simulation from 1980 to 2200 under SSP5-8.5 is used to obtain SSP1-2.6. (b) six MAR simulations forced by six different CMIP models from 1980 to 2100 under a given scenario are used to emulate the corresponding MAR simulation for a 7$^{\text{th}}$ CMIP model. The methods are described in section 2 and the colors used to represent the emulation methods are the same as in Fig. 1. Variable X represents either SMB minus runoff or the surface melt rate.

The median ECS of this 16-model ensemble is 4.2°C, and the ECS of three models out of 16 exceeds 5.0°C, which is high compared to the best estimate of 3.0°C and the 90% confidence interval of 2.0-5.0°C estimated in the IPCC 6$^{\text{th}}$ Assessment Report (Forster et al., 2021). To build a realistic ensemble mean, we therefore attribute weights to individual models, which are the probability of a skew-normal distribution fitted to obtain the 5$^{\text{th}}$, 50$^{\text{th}}$ and 95$^{\text{th}}$ percentiles at ECS of 2.0, 3.0 and 5.0°C (Fig. 7). The corresponding weights are listed in Tab. 1. Despite the imperfect model sampling, the weighted 16-model mean ECS falls from 4.0°C to 3.3°C thanks to weighting, which is closer to the best ECS estimates (Forster et al., 2021) and to the CMIP5 multi-model mean (3.2°C in Meehl et al., 2020). To calculate the percentiles of the weighted distribution, we consider a number of values equal to 100 times the weight for each model, which shifts the multi-model ECS distribution much closer to the ECS very likely range (see small triangles in Fig. 7). We keep the same weights for the ensemble until 2200 even though the 8-model sampling is not as good as a 16-model sampling, giving an ECS weighted mean of 3.7°C (versus 4.4°C for the unweighted mean).

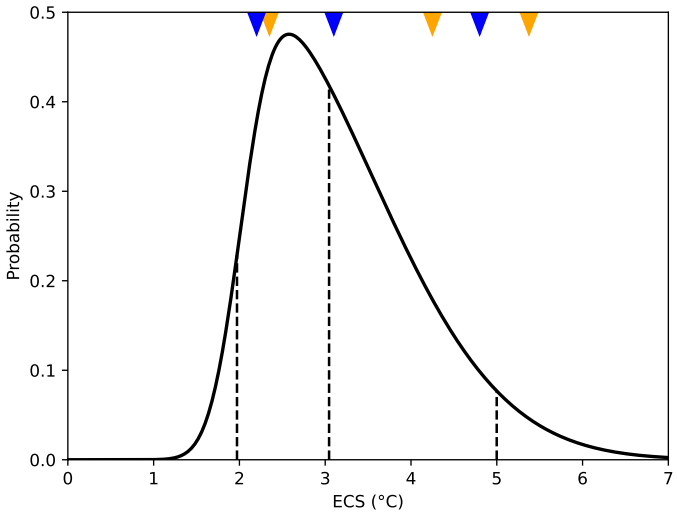

Figure 7. Skew-normal ECS probability (solid line) fitted to obtain its 5th, 50th and 95th percentiles at 2.0, 3.0 and 5.0°C (dashed lines). The orange triangles indicate the 5th, 50th and 95th percentiles of the ECS of the unweighted 16-CMIP model distribution, and the blue triangles show the equivalent for the weighted distribution. The skew-normal distribution was generated using the `skewnorm.pdf` function of the `scipy.stats` package (Virtanen et al., 2020), with a skewness parameter of 5.08, an offset parameter (`loc`) of 2.02°C, and a scale parameter of 1.52.

In the next section, we first use our methodology to estimate the SMB contribution to changes in sea level. As we will see in the next section, very warm conditions may lead to runoff production over the grounded ice sheet, ~~as high as ~~up to elevations of 1000 m ~~high~~above sea level, and a large part of the melt water not retained in the firn is expected to drain ~~into~~ onto ice shelves located downstream (Kingslake et al., 2017). We therefore assume that all ~~liquid water in excess~~ excess liquid water over the grounded ice sheet flows to the ice shelves downstream or directly into the ocean. Therefore, as far as the grounded ice sheet is concerned, the production of liquid water beyond firn saturation is considered as runoff, i.e., a negative term in our SMB calculations.

We then use our methodology to estimate when the surface conditions have the potential to trigger ice shelf hydrofracturing. As discussed previously, melt rates can be too low to saturate the firn with liquid water, which is why we consider that a necessary condition for hydrofracturing has to be based on the production of ~~liquid water in excess~~ excess liquid water and not on melt rates as done in previous studies (e.g., Trusel et al., 2015; Nowicki et al., 2020; Seroussi et al., 2020). The relatively flat ice shelves are treated in a different way than the grounded ice. Indeed, in addition to the liquid water produced locally, the ice shelves receive the liquid water that was produced beyond firn saturation over the upstream grounded ice sheet. To account for this, we assume that an ice shelf receives a fraction of the liquid water produced over the grounded ice of its drainage basin. The fraction is taken as the fraction of the basin coastline occupied by the ice shelf.

Another specificity of ice shelves is that they are relatively flat and can bend, so that it is impossible to estimate the amount of liquid water forming ponds or flowing into the ocean without a dedicated hydrology–firn–ice-shelf model. This is why we

introduce an empirical threshold on the production rate of ~~liquid water in excess~~ excess liquid water to assess the potential for hydrofracturing. The idea is to have a rate that is sufficiently high to form ponds and fill crevasses even if a part flows into the ocean. The average production of ~~liquid water in excess~~ excess liquid water over Larsen B prior to its collapse was estimated between 200 and 300 $\mathrm{kg\,m^{-2}\,yr^{-1}}$ (Holland et al., 2011; van Wessem et al., 2016; Costi et al., 2018), so our threshold has to be lower than that. There is nonetheless a large uncertainty on the threshold and we sample it in a normal distribution of 150 and 61 $\mathrm{kg\,m^{-2}\,yr^{-1}}$ of mean and standard deviation, respectively. This is chosen to obtain 90% of the threshold values between 50 and 250 $\mathrm{kg\,m^{-2}\,yr^{-1}}$. The lower end of this range is chosen empirically so that not too many ice shelves are above the threshold in present-day conditions. The uncertainty on the threshold is hence included in the calculation of the probability of a given ice shelf to be over the threshold.

In the next section we present our results as confidence intervals, which we define as in the IPCC reports: ~~17—83th~~ 17th–83th percentiles for the likely range (66% probability) and ~~5–95th~~ 5th–95th percentiles for the very-likely range (90% probability). These percentiles account for the uncertainty ~~on~~ of the CMIP models weighted to account for the likelihood of their ECS, and ~~on the uncertainty on~~ for the uncertainty of the threshold on liquid water production in excess when we investigate the potential for ice shelf hydrofracturing.

3 Ensemble of projections from 1850 to 2200

Here we use the emulated ensemble to estimate the SMB evolution over the grounded ice sheet from 1850 to 2200 and the equivalent changes in sea level (section 3.1), and the production of ~~liquid water in excess~~ excess liquid water from 1850 to 2200 and the implications for ice shelf hydrofracturing (section 3.2). Importantly, our estimates of sea level projections only contain the part related to SMB variations, and not the contribution from the ice sheet dynamics which is driven by ocean-induced melting and hydrofracturing. In Appendix E, we also describe the SMB evolution over ice shelves.

3.1 Grounded ice sheet and sea level

First of all, our emulated ensemble indicates that the grounded ice sheet SMB was 110 $\mathrm{Gt\,yr^{-1}}$ lower in 1850–1869 than in 1995–2014 and increased slowly through the 20$^{\mathrm{th}}$ century (Fig. 8). In comparison, a combination of ice cores and simulations from another regional climate model gave $\sim$200 $\mathrm{Gt\,yr^{-1}}$ of difference between these two periods (Thomas et al., 2017). This increasing SMB in our emulation is equivalent to a reduction of 1.3 cm of global mean sea level from 1900 to 2010 (likely range: 0.4 to 2.2 cm) with respect to the 1891–1910 mean (i.e., assuming that the climatological SMB over 1891–1910 contributed to zero sea level rise).

Our projections over the grounded ice until 2100 agree quite well with previous estimates of sea level contribution reported by the IPCC for the three scenarios, and are slightly lower than previous estimates for the unweighted CMIP6 ensemble (Tab. 3). We estimate a median SMB mitigation of sea level rise between 2.0 and 5.0 cm depending on the scenario. As in Kittel et al. (2021), the three SSP scenarios diverge after 2040: the SSP1-2.6 SMB remains $\sim$100 $\mathrm{Gt\,yr^{-1}}$ above 1995–2014, the SSP2-4.5 SMB keeps increasing until 2100 at a rate similar to 1970–2014, and the SSP5-8.5 SMB increases 1.7 times faster than SSP2-4.5 until 2100 (Fig. 8).

For seven out of eight models going beyond 2100, the maximum SMB over the grounded ice sheet is reached between 2090 and 2120 under SSP5-8.5 and a few decades earlier under SSP1-2.6 (Fig. 9). Under SSP1-2.6, the SMB over the grounded ice sheet goes back to present-day values during the 22$^{\mathrm{nd}}$ century. Under SSP5-8.5, the three models with an ECS lower than 4°C predict ~~a~~ an SMB that remains ~~over~~ above the present-day value until 2200. In contrast, four models predict that increasing runoff over the grounded ice sheet will overwhelm increasing accumulation, with ~~a~~ an SMB decreasing below the present-day value after 2035 to 2075 depending on the model. It cannot be ruled out that the grounded ice sheet reaches a net surface mass loss near 2200, although this is extremely unlikely given that the two models crossing or approaching this limit are above the 95$^{\mathrm{th}}$ percentile at the end of the 21$^{\mathrm{st}}$ century.

In terms of sea level, the net contribution of the Antarctic SMB over 2000–2200 is between -10 and -1 cm for SSP1-2.6 and between -33 and +6 cm for SSP5-8.5 (Tab. 4). Interestingly, the relative importance of sea level reduction between SSP1-2.6 and SSP5-8.5 is reversed for the two models producing the largest amount of runoff in the 22$^{\mathrm{nd}}$ century (MAR–CanESM5 and MAR–CESM2-WACCM) compared to the other models. This is due to the massive runoff production over the grounded ice sheet after 2150 under SSP5-8.5 in these two models, which counterbalances the excess of accumulation before 2150 (Fig. 9). MAR–CanESM5 even has a net positive contribution to sea level rise over the two centuries under SSP5-8.5.

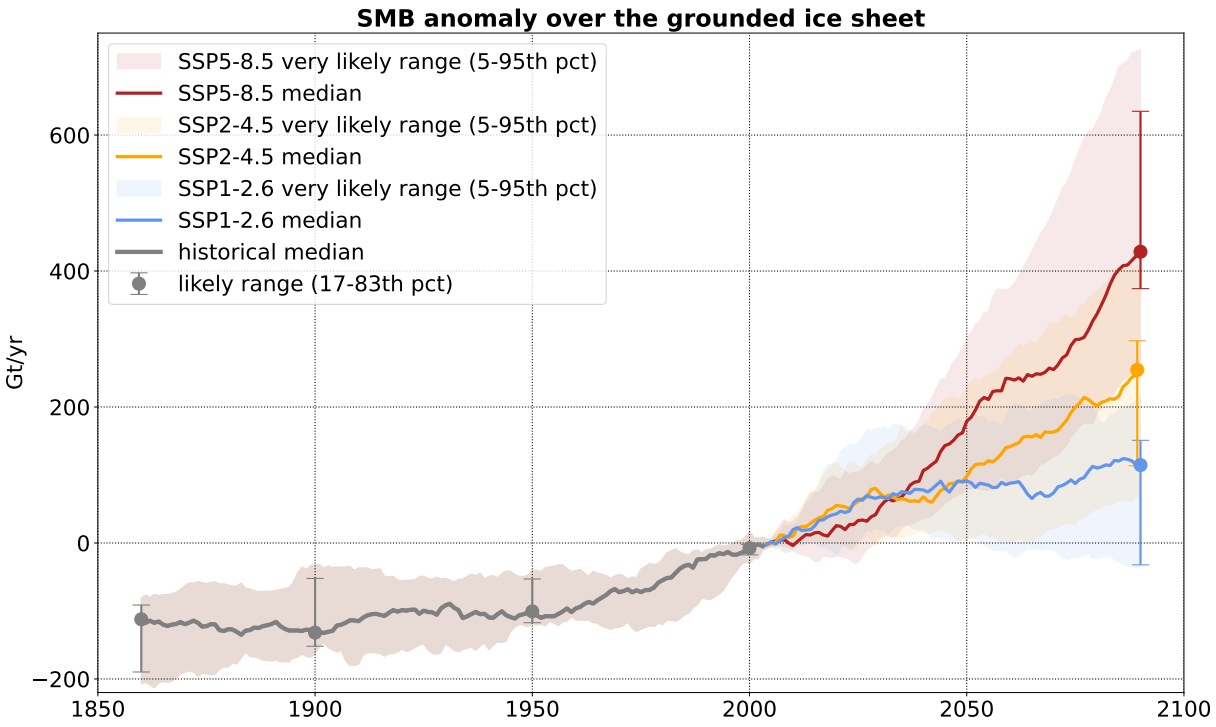

Figure 8. Emulated ensemble of surface mass balance over the grounded Antarctic ice sheet for the historical period and three SSP scenarios. The median and percentiles are calculated based on the 16-model ensemble weighted to match with the very likely range of ECS (see section ??2.1). A 21-year running average has been used for all the time series.

Table 3. Projected sea level contributions (in cm) from the Antarctic Ice Sheet SMB from 2000 to 2099 (relative to 1995–2014, i.e. assuming that the mean SMB over that period yields no sea level rise), for the three selected SSP scenarios, shown as median (likely range, i.e., 17–83th percentile) [very likely range, i.e., 5–95th percentile]. The IPCC-AR5/6 estimates are those presented in Tab. 9.3 of IPCC-AR6 (Fox-Kemper et al., 2021), i.e., recalculated for the SSP scenarios from IPCC-AR5, and originally derived from the CMIP5 global mean surface air temperature using a linear accumulation-temperature relationship (Church et al., 2013). The data of Kittel et al. (2021) are statistical reconstructions based on the air temperature averaged south of 60°S for 33 CMIP6 models, and the percentiles have been recalculated for this table.

Study	SSP1-2.6	SSP2-4.5	SSP5-8.5
IPCC AR5/6	–2 (–3 to –1) [-4 to -1]	–3 (–4 to –2) [-6 to -1]	–5 (–7 to –3) [-9 to -2]
CMIP6 estimate by Kittel et al. (2021)	-2.6 (-4.0 to -1.6) [-4.8 to -1.1]	-3.9 (-5.2 to -2.5) [-5.9 to -1.8]	-5.7 (-8.1 to -3.8) [-8.7 to -3.2]
This study	-2.0 (-3.4 to -0.1) [-4.1 to 0.1]	-3.2 (-4.4 to -1.4) [-6.1 to -0.5]	-5.0 (-7.8 to -4.0) [-8.8 to -2.6]

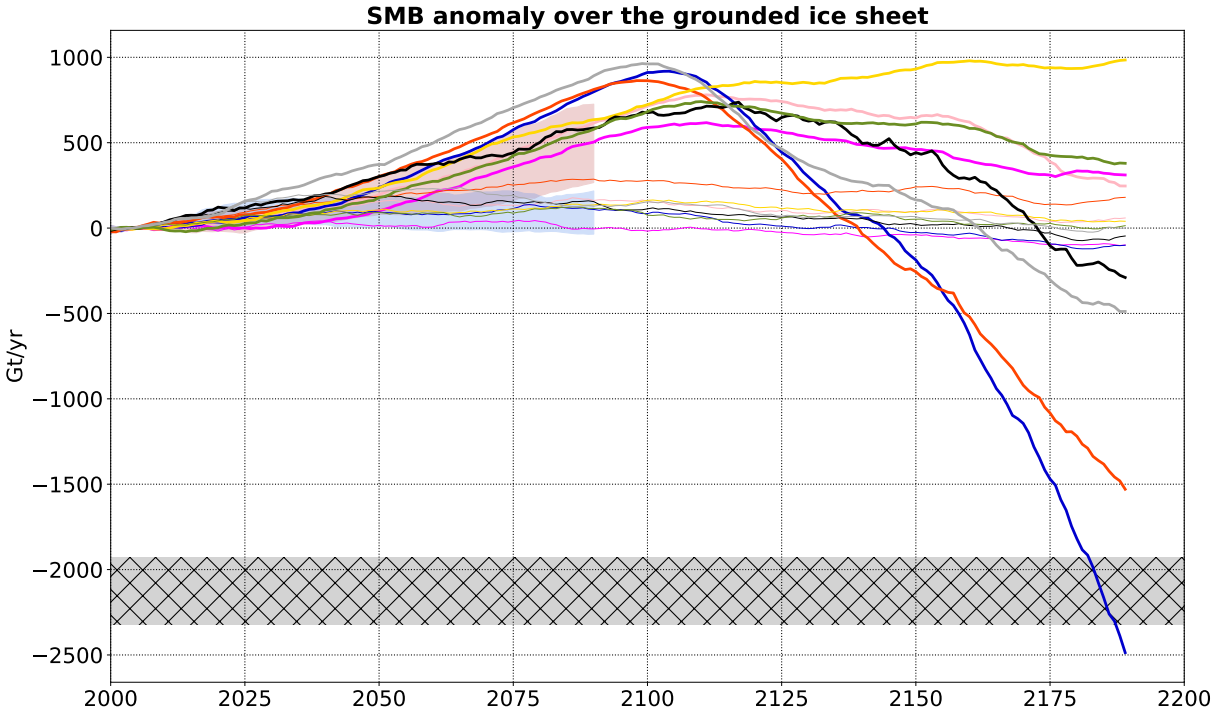

Figure 9. Eight emulations of surface mass balance over the grounded Antarctic ice sheet for the SSP-1.26 and SSP5-8.5 scenarios. The very likely range from 16 emulations over 2000–2100 (same as Fig. 8) is also shown. The hatched area indicates the anomaly interval at which SMB reaches zero, according to the MAR, RACMO and HIRHAM present-day values reported in Mottram et al. (2021). A 21-year running average has been used for all the time series.

In terms of patterns, the projected increase in SMB over the grounded ice sheet until 2100 is largest along the coast of the Bellingshausen and Amundsen seas, as well as in ~~Dröning~~ Dronning Maud Land (Fig. 10). The models producing large amounts of runoff by 2200 under SSP5-8.5 tend to have lower SMB than presently below 1000 m above sea level, i.e. along the coastline and upstream of many ice shelves (Fig. 11).

3.2 Ice shelves and hydrofracturing potential

We now investigate the years of emergence of surface conditions that make ice shelves prone to hydrofracturing, keeping in mind that mechanical conditions would also be necessary for the developments of fractures (see Introduction). As explained in section 2.1, we use a threshold on the production rate of liquid water beyond firn saturation to identify such conditions.

According to our estimates, a few ice shelves were already likely (Fig. 12) or very likely (Fig. 13) in conditions favorable to hydrofracturing before 2015, and sometimes since the 19$^{\text{th}}$ century. This is the case of Larsen A and B that collapsed in 1995 and 2002 (Rott et al., 1996, 2002) after a progressive thinning that led to favorable mechanical conditions for fractures (Shepherd et al., 2003).

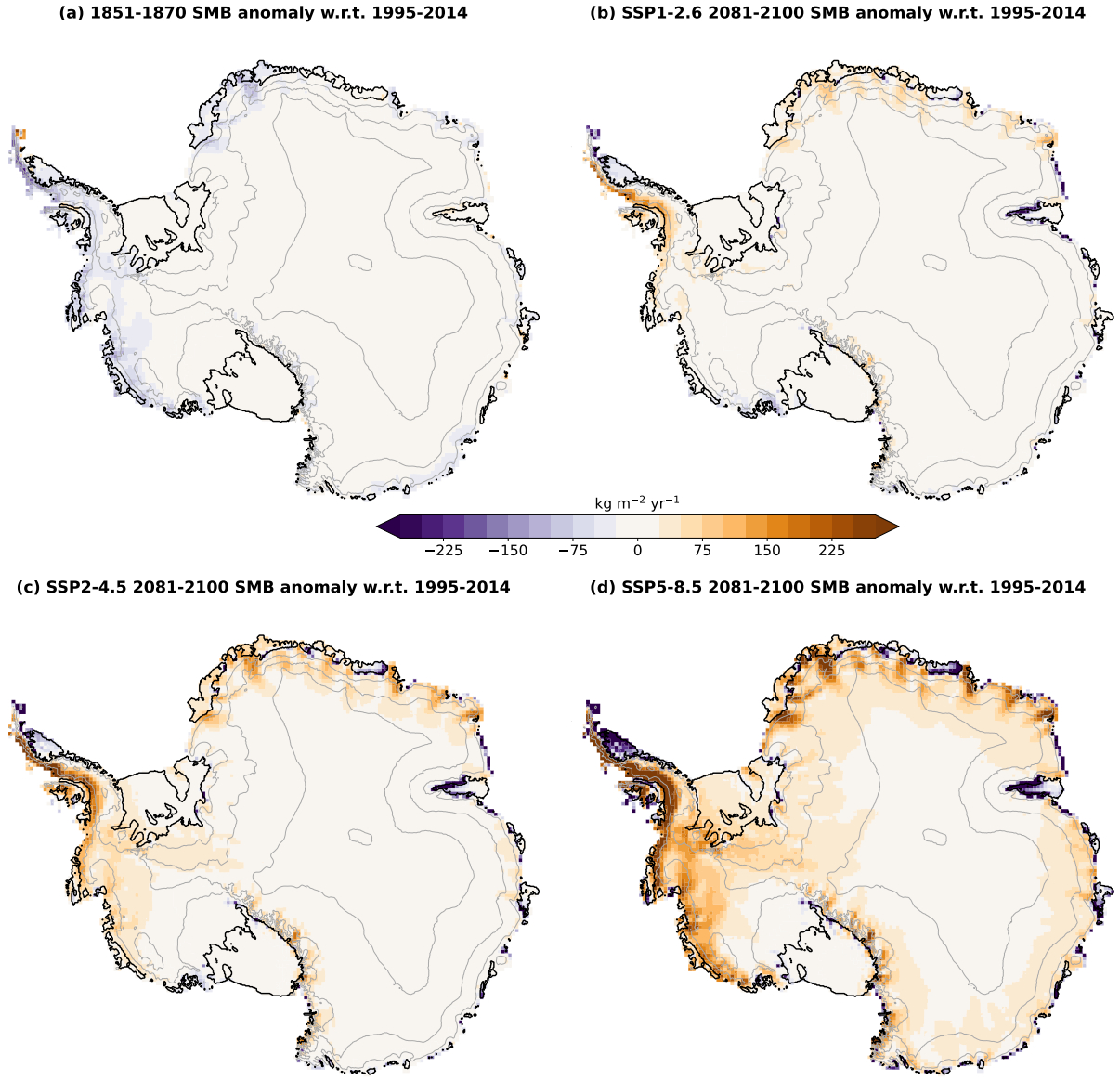

Figure 10. Weighted mean SMB anomaly for four different periods or scenarios with respect to the average SMB over 1995–2014. This was calculated from the 16 models listed in Tab. 1. The grey contours indicate the topography (every 1000 m) and the black contours show the ice shelves.

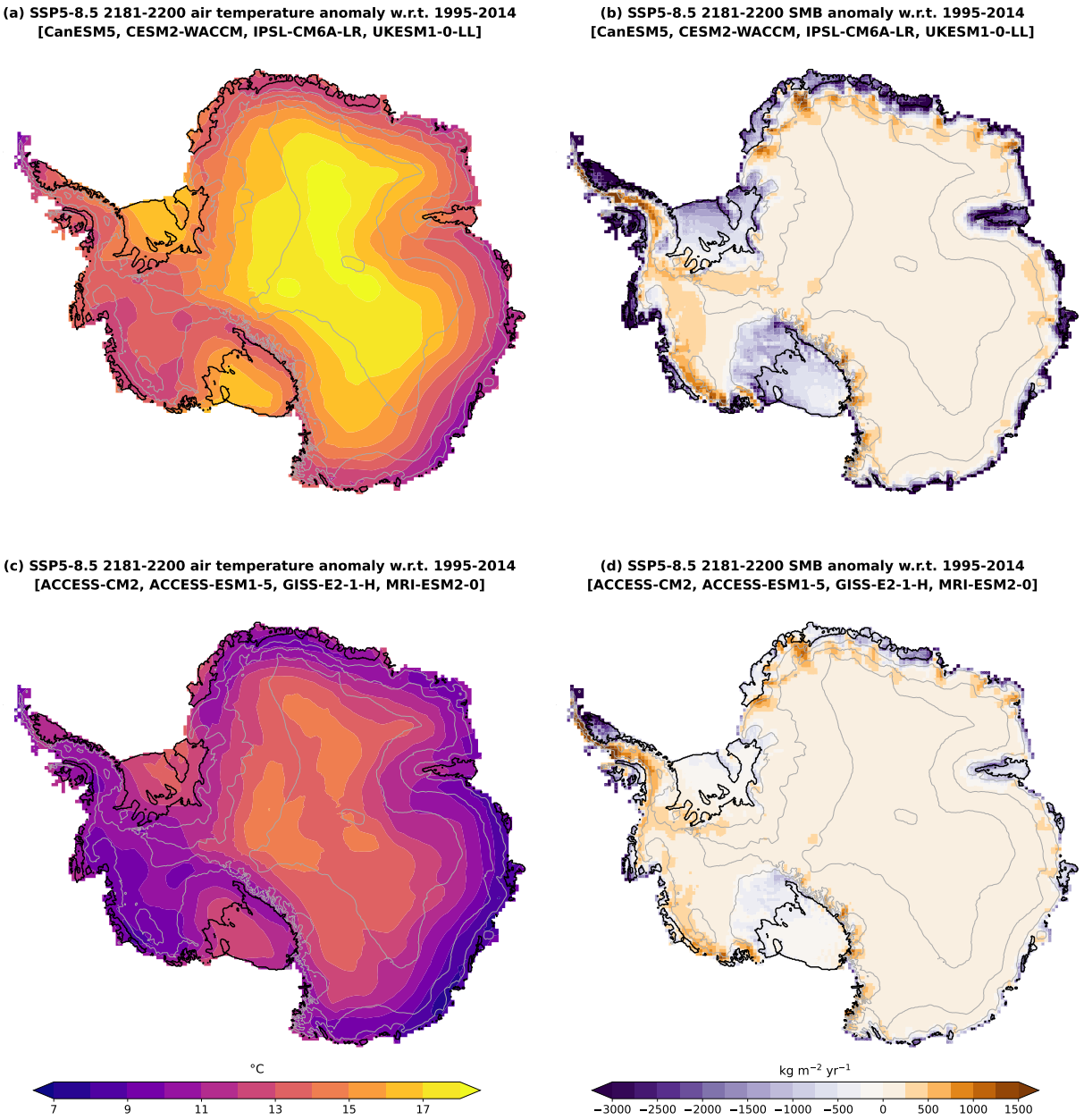

Figure 11. Mean 2181–2200 ~~surface~~ near-surface air temperature (left panels) and SMB (right panels) anomaly under SSP5-8.5 with respect to the 1995–2014 mean, for the four models with the most negative SMB spatially integrated anomaly (upper panels) and the four models with the least negative spatially integrated SMB anomaly (lower panels). This was calculated from the 8 models of Tab. 1 that are available until 2200, with equal weight for all models. The grey contours indicate the topography (every 1000 m) and the black contours show the ice shelves.

Table 4. Projected sea level contributions (in cm) from the Antarctic Ice Sheet SMB from 2000 to 2200 (relative to 1995–2014).

Model	SSP1-2.6	SSP5-8.5
MAR–ACCESS-CM2	-5.3	-22.7
MAR–ACCESS-ESM1-5	1.1	-17.5
MAR–CanESM5	-1.3	6.0
MAR–CESM2-WACCM	-10.3	-0.6
MAR–GISS-E2-1-H	-4.8	-32.9
MAR–IPSL-CM6A-LR	-4.0	-16.9
MAR–MRI-ESM2-0	-3.2	-22.2
MAR–UKESM1-0-LL	-5.7	-15.8

Further south in the Antarctic Peninsula, Larsen C, Wordie and Wilkins have a likely range starting in the 1980s (Fig. 12) but extending towards the end of the 21st century. This considerable spread indicates present-day rates of liquid water production close to the threshold distribution. These three ice shelves are actually known for their recent evolution and wet surface conditions: the Wilkins Ice Shelf progressively thinned (Braun et al., 2009) before a partial disintegration in 2008 likely due to hydrofracturing (Scambos et al., 2009), the Wordie Ice Shelf progressively broke up from 1991 to 2009 (Doake and Vaughan, 1991; Cook and Vaughan, 2010), and the Larsen C Ice Shelf lost 25-30% of its area from the 1970s to 2021 (Cook and Vaughan, 2010; Greene et al., 2022). Also in the Peninsula, the George VI Ice Shelf has a likely range starting at the end of the 19th century. Melt ponds have been reported on George VI since the 1960s (Wager, 1972; Bell et al., 2018; Banwell et al., 2021) but the ice shelf compressive stress does not promote ice shelf fractures (LaBarbera and MacAyeal, 2011), even though the ice shelf lost 8% of its area from 1947 to 2010 (Cook and Vaughan, 2010).

After the Peninsula, the region where ice shelves are most prone to hydrofracturing in terms of surface conditions is the Indian Ocean sector of East Antarctica. The ice shelves in Vincennes Bay, East Antarctica, are estimated to be in similar surface conditions as Larsen A and B (Fig. 12). These ice shelves have been covered by supraglacial lakes (Arthur et al., 2020), and their extent has decreased by $\sim$10% over the two first decades of the 21st century (Greene et al., 2022), but no widespread break-up has been observed so far. The Publications, Shackleton and Moscow University ice shelves have a likely range starting before 2025, and widespread melt ponds or aquifers are observed in present-day conditions (Kingslake et al., 2017; Bell et al., 2018; Alley et al., 2018; Stokes et al., 2019; Arthur et al., 2020, 2022; Saunderson et al., 2022), again with no significant break-up reported recently. The Amery ice shelf, as well as Roi Baudouin and Nivl, further west in Dronning Maud Land, currently often covered with ponds or aquifers (Alley et al., 2018; Spergel et al., 2021; Arthur et al., 2022; Priya et al., 2024; Dell et al., 2024), have their likely range starting in $\sim$2050 for any scenario (Fig. 12).

The fate of the other ice shelves beyond 2050 is very much dependent on the emission scenario (Fig. 12). Under the SSP5-8.5 scenario, the number of ice shelves likely prone to hydrofracturing increases from 13 ± 6 to all of the 56 ~~monitored~~ considered ice shelves from 2050 to 2150. In contrast, this number only increases from 11 ± 4 to 16 ± 9 under SSP1-2.6, meaning that a

majority of ice shelves are unlikely to experience hydrofracturing in this scenario. Under SSP2-4.5, we find that hydrofracturing conditions are likely not met before 2100 for 21 of the 56 ~~monitored~~ considered ice shelves (Fig. 14).

The giant Ross and Ronne-Filchner ice shelves are unlikely to experience hydrofracturing before the early 22nd century in SSP5-8.5, ~~as found in other studies (Kuipers Munneke et al., 2014; Dunmire et al., 2024; Veldhuijsen et al., 2024), with the exception of van Wessem et al. (2023) who found that Ross could become prone to hydrofracturing before 2100.~~ consistently with previous studies (Kuipers Munneke et al., 2014; van Wessem et al., 2023; Dunmire et al., 2024; Veldhuijsen et al., 2024). In the Amundsen Sea, the ice shelves from Thwaites to Getz are also unlikely to experience hydrofracturing before the early 22nd century, consistently with the projections of Donat-Magnin et al. (2021) and with the little change in firn air content by 2100 reported by Dunmire et al. (2024) and Veldhuijsen et al. (2024).

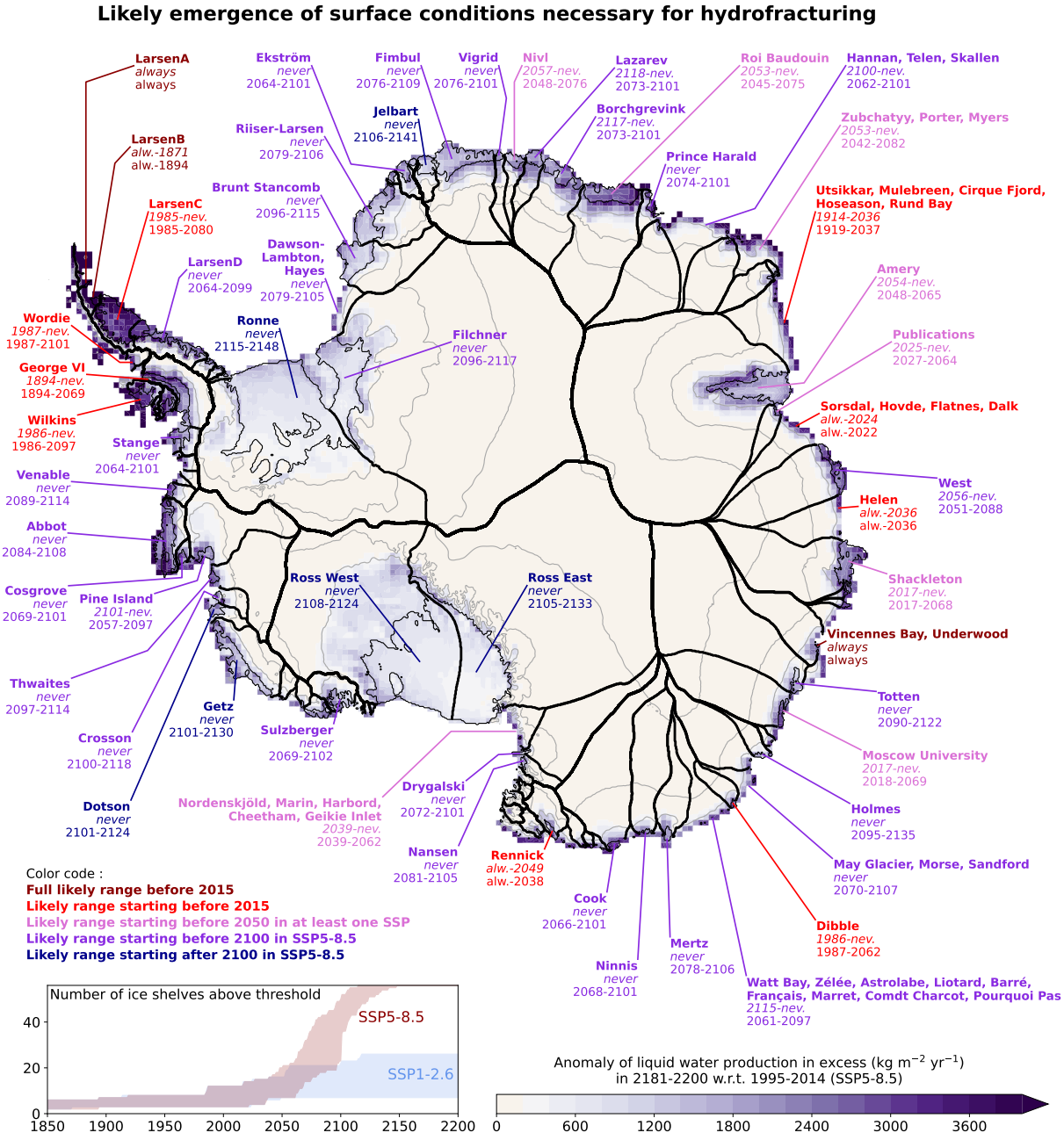

Figure 12. Time intervals at which the likely (17–83th percentiles) production of excess liquid water ~~in excess~~ likely exceeds the threshold that makes hydrofracturing possible (see text), for 56 ice shelves or groups of ice shelves. The first time range, in italic, corresponds to SSP1-2.6, while the second range corresponds to SSP5-8.5. The estimated years are based on the weighted 16-model ensemble until 2100 and on the weighted 8-model ensemble from 2101 to 2200. Indications of "always" and "never" have to be understood as between 1850 and 2200 (e.g., "never" means either after 2200 or never). The background map shows the eight-model mean anomaly of liquid water production beyond firn saturation at the end of the 22nd century. The topography contours are in grey (every 1000 m) and the ice shelves are delineated in thin black. The contours of the drainage basins of individual ice shelves is in thick black (from Mouginot et al., 2017 and Rignot et al., 2019).

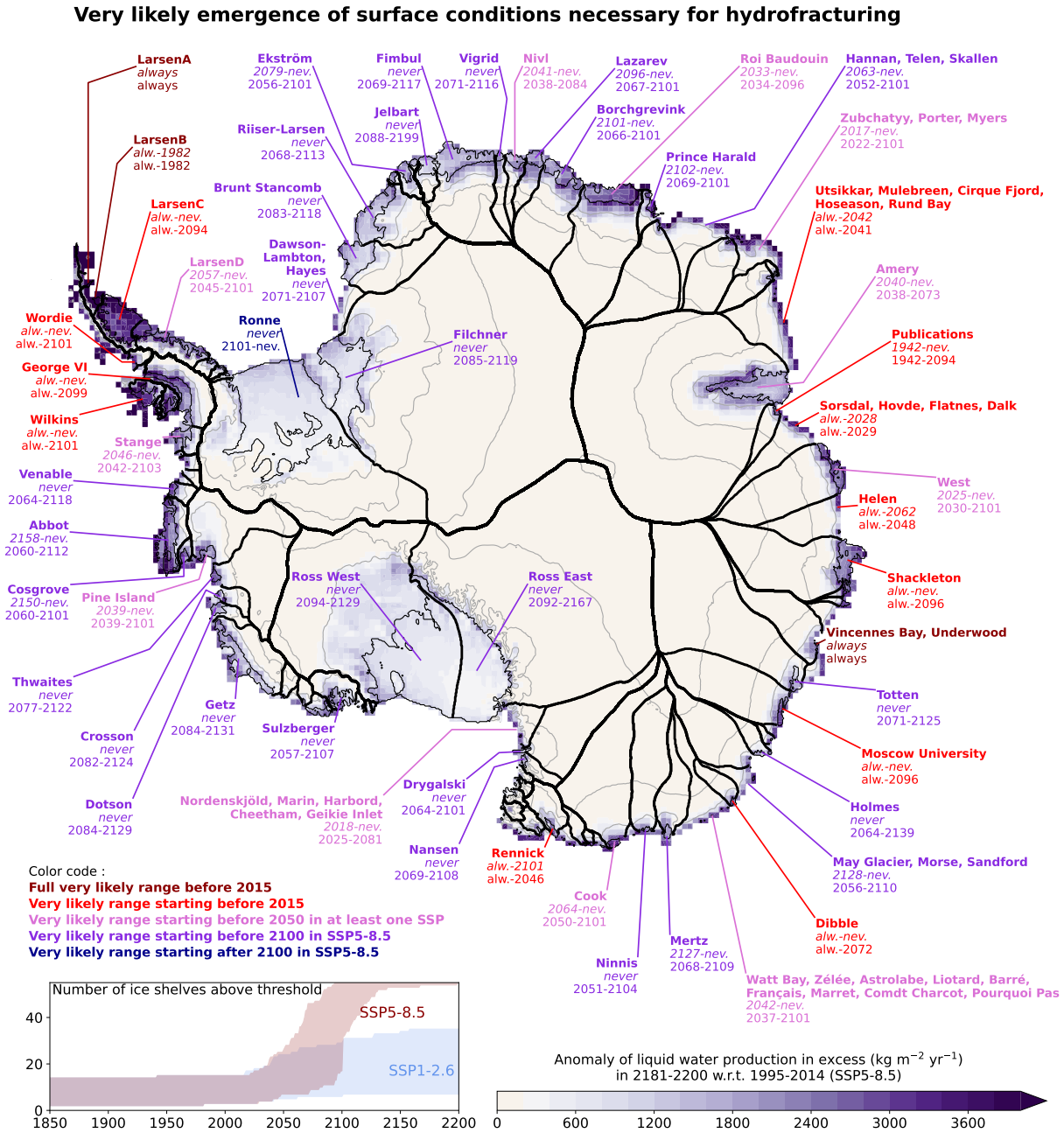

Figure 13. Same as Fig. 12 but for the very likely range (5–95$^{\text{th}}$ percentiles).

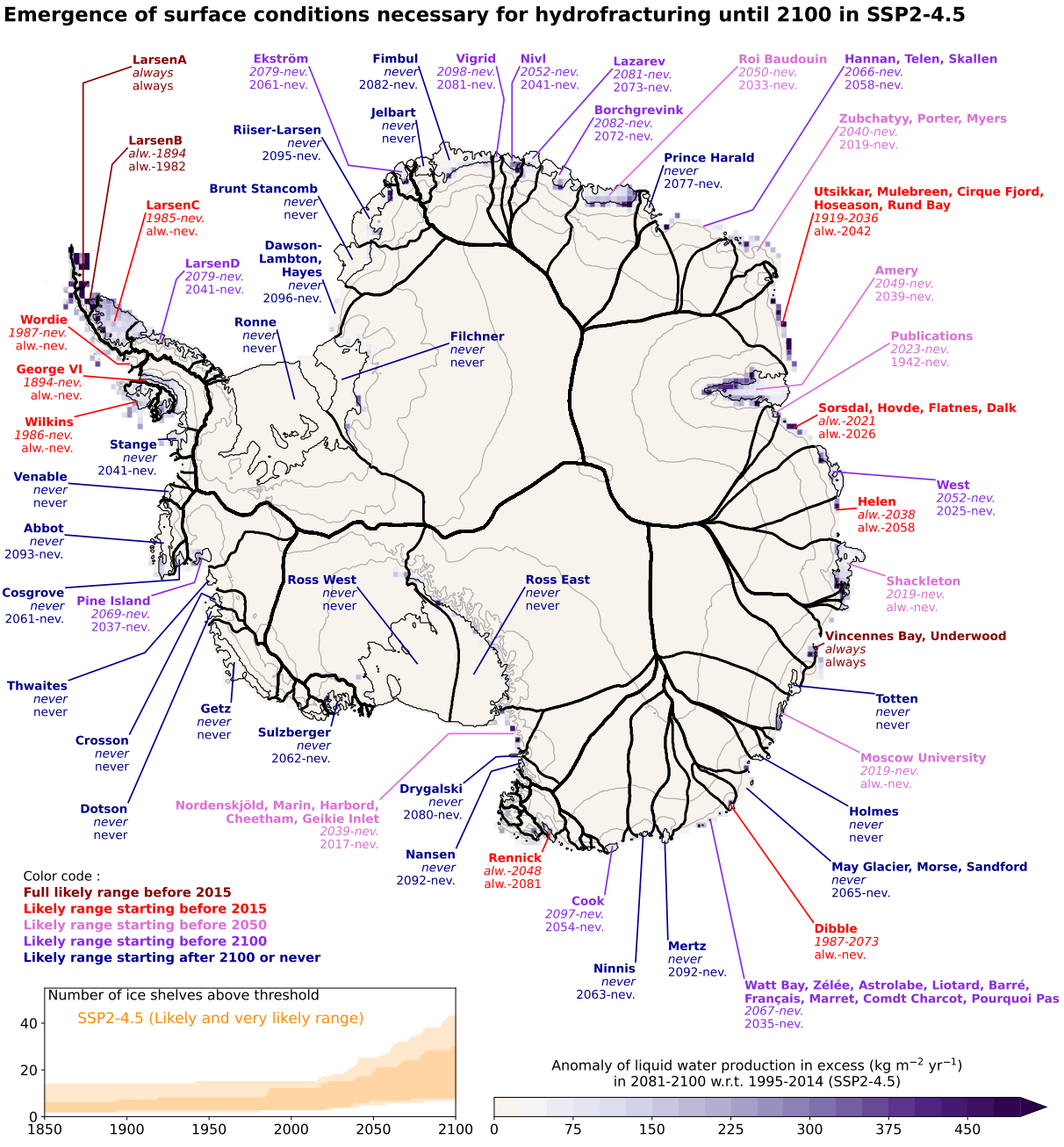

Figure 14. Similar to Fig. 12 but for the SSP2-4.5 scenario. The dates in italic give the likely range (17–83$^{\text{th}}$ percentiles) and the others give the very likely range (5–95$^{\text{th}}$ percentiles). The background map shows the 16-model mean anomaly of liquid water production beyond firn saturation at the end of the 21$^{\text{st}}$ century under SSP2-4.5.

4 Discussion

In this study, we have used a relatively simple model to emulate RCM simulations. It is based on exponential fits for snow melt and accumulation rates. Although the method gives reasonably good results, we suggest that more complex fitting methods, in particular through deep learning algorithms fed by multiple CMIP model variables (e.g., Sellevold and Vizcaino, 2021; van der Meer et al., 2023), may improve our approach. A complex algorithm trained on regional climate simulations with complex physical parameterisations may be able to represent aspects that are not accounted for in our simple statistical–physical model, such as the emergence of bare ice and its effect on albedo, the presence of ice slabs in the firn, the effects of rainfall, the melt-elevation feedback, or radiative feedbacks associated with the evolution of the cloud phase. Combining our methodology with a downscaling approach (e.g. Noël et al., 2023) may also improve the emulated data. For any method, the results presented in section 2.3.5 stress the importance of using a training dataset made of RCM simulations driven by multiple CMIP models for obtaining robust results.

In this work, we have also assumed an instantaneous saturation of the firn beyond certain melt rates, while it can take an infinite amount of time to saturate it if melt rates are just above the threshold (e.g., Donat-Magnin et al., 2021). This could be addressed by introducing the temporal evolution of the depleted firn air volume in our simple model or in the deep learning approach, or in a simpler way, by introducing some time lag in the relationship between melt and firn saturation.

Our approach has consisted of emulating MAR simulations. Other RCMs, possibly combined ~~to~~ with elaborated firn models, have similar skills in representing typical Antarctic conditions (Mottram et al., 2021), but there is ~~likely~~ a considerable spread in their response to surface warming (Glaude et al., 2024). For example, the depth and vertical resolution of firn models probably make important differences in the timing of runoff production. The 20-m firn layer simulated in MAR thus likely reaches liquid water saturation earlier than models with a thicker firn layer. One of the next priorities will therefore be to emulate the diversity of RCM or firn models sensitivities, which would make the uncertainty ranges much more comprehensive. The absence of physical representation of ponding and horizontal routing of liquid water nonetheless remains a major caveat of all current RCMs. Another important limitation of RCMs is the use of a constant ice sheet elevation, although the melt–elevation feedback seems to become important only after 2200 in the SSP5-8.5 scenario (Coulon et al., 2023).

Here we have weighted the CMIP models to represent the very likely ECS distribution. We consider this as an improvement compared to unweighted multi-model means, but more comprehensive weighting approaches should be explored. For example, weights based on misfits with observational data can reduce the uncertainty (Gorte et al., 2020; Coulon et al., 2023). Given the importance of internal variability for conditions at the surface of ice shelves (Tsai et al., 2020), it is nonetheless important to use multiple members of a given CMIP model in the weighting process, and our method can be used to emulate all the ensemble members of individual CMIP experiments (Caillet et al., 2024).

5 Conclusions

We have presented a novel mixed statistical-physical approach to emulate the spatio-temporal variability of the MAR regional climate model. We have focused on surface mass balance and on the production of liquid water beyond firn saturation. We

have presented evidence that this method can be used to extend existing MAR simulations to other periods and scenarios that were not originally processed through MAR. Our method is also able to emulate MAR simulations driven by CMIP models that have never been used to actually drive MAR simulations.

Our method is useful to populate ensembles of surface mass balance and production rates of liquid water which are needed to constrain ice sheet model ensembles and to estimate the likely range of future sea level rise. This approach has been applied to complete the set of RCM simulations used to drive ice sheet simulations until 2150 in the PROTECT European project (Durand et al., 2022; Mosbeux et al., 2024). This could also be useful for the upcoming ISMIP exercise as it is relatively simple to use, can be applied before obtaining all the CMIP 6-hourly data, and can provide the information needed to trigger the hydrofracturing mechanism in ice sheet models.

Here we have used this method to ~~built~~ build an ensemble of projections from 1850 to 2200 under several scenarios, in combination with a weighting method to correct the likely ECS distribution which is poorly represented by the CMIP6 ensemble. We believe that most original aspects of our projections compared to recent studies (van Wessem et al., 2023; Dunmire et al., 2024; Veldhuijsen et al., 2024) are (i) the time coverage back to 1850 and until 2200 while other studies cover ∼1980-2100, (ii) the use of a large weighted ensemble of CMIP models to account for ~~the models~~ their uncertainty while keeping a plausible equilibrium climate sensitivity, (iii) the relatively large number of MAR simulations used to assess and calibrate our simple emulator.

We find a likely SMB contribution to sea level rise of 0.4 to 2.2 cm from 1900 to 2010, and -3.4 to -0.1 cm from 2100 to 2099 in SSP1-2.6, versus -4.4 to -1.4 cm in SSP2-4.5 and -7.8 to -4.0 cm in SSP5-8.5. Based on a smaller ensemble, we find a considerable uncertainty in the SMB contribution to sea level from 2000 to 2200: between -10 and -1 cm for SSP1-2.6 and between -33 and +6 cm for SSP5-8.5.

We have then defined a criterion to identify the timing of surface conditions that make ice shelves prone to hydrofracturing. The emergence of such conditions over the historical period and in the near future qualitatively matches with observations of melt ponds and aquifers on a number of ice shelves. While the majority of ice shelves could remain safe from hydrofracturing in the SSP1-2.6 scenario, we estimate that all the Antarctic ice shelves will very likely be prone to hydrofracturing before 2150 in the SSP5-8.5 scenario. In combination with the ice shelf mechanical weakening induced by ocean warming (e.g., Naughten et al., 2023; Mathiot and Jourdain, 2023), increased surface runoff is a major threat for the Antarctic ice shelves and for the grounding ice sheet outflows that they currently restrain.

Code and data availability. The tools used to emulate the RCM data are available on https://github.com/nicojourdain/extend_SMB_melt_runoff.

Appendix A: Evaluation of present day MAR simulations

The surface mass balance and melting conditions produced by MAR have been evaluated in comparison to observational products in several studies. Agosta et al. (2019) used firn-core SMB estimates to evaluate a MAR configuration covering the entire ice sheet: their SMB spatial pattern was well captured and the mean bias was 4%. Donat-Magnin et al. (2020) compared their MAR configuration of the Amundsen Sea sector to automatic weather stations, airborne-radar and firn-core SMB, melt days from satellite microwave, and melt rates from satellite scatterometer. They obtained good results for near-surface temperatures (mean overestimation of 0.1°C), near-surface wind speeds (mean underestimation of 0.42 $\mathrm{m\,s^{-1}}$ and SMB (local biases lower than 20%). The mean surface melt rate over the Amundsen Sea region was underestimated by 18% but the interannual variability was well captured for both melt rate and the annual number of melting days. The aforementioned MAR simulations were forced by atmospheric reanalyses and Kittel et al. (2021) showed that as far as SMB was concerned, MAR forced by climate models was close to MAR forced by the ERA5 reanalysis over the recent decades.

Here we assess the present-day production of liquid water beyond firn saturation in a similar way as van Wessem et al. (2023) did with the RACMO model, i.e., in comparison to an observational estimate of melt pond volume derived from Sentinel 2 data. This is a qualitative assessment as neither MAR nor RACMO simulate ponding (they remove the excess of liquid water and do not simulate horizontal transport of liquid water). We find that the areas of high liquid water production in MAR generally correspond to the areas where high melt pond volumes are estimated from Sentinel 2 data (van Wessem et al., 2023, Their Extended Data Fig. 3), even if the area of high runoff over Larsen C is larger than the area of large melt pond volume in the satellite product (Fig. A1).

Appendix B: Rationale for neglecting rainfall in the emulation

In the emulation method described in section 2.3, we have assumed that precipitation is entirely made of snow and that the excess liquid water only originates from surface melting. This means that rainfall has been neglected and this section provides further motivation for this assumption as well as an evaluation of the resulting error.

The only RCM simulation that we have until 2200 (MAR–IPSL-CM6A-LR, SSP5-8.5) indicates that precipitation mostly consists of snowfall all along the 21$^{\mathrm{st}}$ century (Fig. B1). At 2100, the total precipitation includes 3% of rainfall over the grounded ice and 12% over the ice shelves. The proportion of rainfall increases along the 22$^{\mathrm{nd}}$ century to reach 14% over the grounded ice and 43% over the ice shelves at 2200. Interestingly, from 1980 to 2200, rainfall always represents 10% to 20% of the surface melt rate, for both the grounded ice and the ice shelves (Fig. B1).

To assess the impact of non-zero rainfall, we use the Appendix B of Donat-Magnin et al. (2021), in which it is demonstrated that liquid water is produced beyond firn saturation if:

$$\frac{\mathrm{MLT}+\mathrm{RF}}{\mathrm{SNF}-\mathrm{MLT}} > \frac{\rho_{\mathrm{co}}}{\rho_{\mathrm{s}}} - 1 \tag{B1}$$

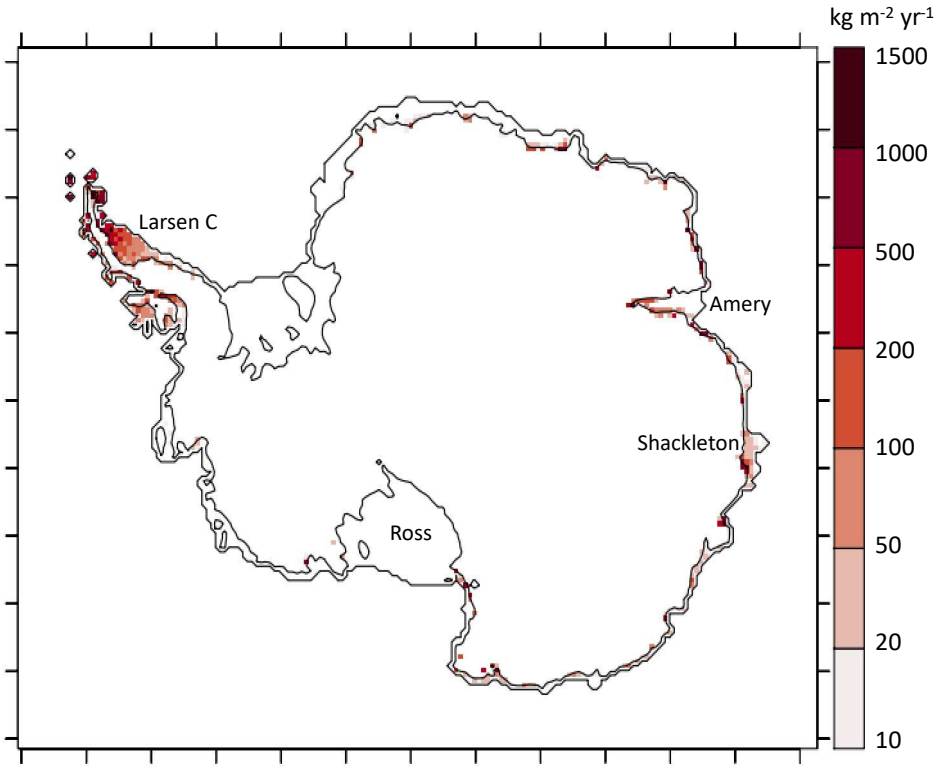

Figure A1. Average production of liquid water beyond firn saturation ($\mathrm{kg\,m^{-2}\,yr^{-1}}$) in MAR driven by the ERA5 reanalysis, over 2015–2022.

where MLT is the surface melt rate, SNF the snowfall rate, RF the rainfall rate, ρ_{co} the firn close-off density (830 $\mathrm{kg\,m^{-3}}$ in the following), and ρ_s the fresh snow density (300 $\mathrm{kg\,m^{-3}}$ in the following). If RF = 0, Eq. B1 becomes Eq. 3 with $r = (\rho_{co} - \rho_s)/\rho_{co} = 0.64$.

First, let us consider the impact of neglecting rainfall before melting as a source of liquid water in the firn. At most, rainfall reaches RF = 0.20 MLT (Fig. B1) and in this case, Eq. B1 can be rewritten as:

$$\frac{\mathrm{MLT}}{\mathrm{SNF}} > \frac{\rho_{co} - \rho_s}{\rho_{co} + 0.2\,\rho_s} \tag{B2}$$

Hence, accounting for rainfall is equivalent to having an effective r threshold of 0.60 instead of 0.64, which has a relatively small effect (see sensitivity to r in Fig. 2).

Second, let us consider the consequence of having a precipitation that is partly liquid, assuming that the Clausius-Clapeyron relationship (Eq. 1) is valid for the total precipitation. For the ice shelves at year 2100, we can write RF = 0.12 PR and SNF = 0.88 PR (Fig. B1b), where PR is the total precipitation rate. In this case, Eq. B1 becomes:

$$\frac{\mathrm{MLT}}{\mathrm{PR}} > \frac{0.88\,\rho_{co} - \rho_s}{\rho_{co}} \tag{B3}$$

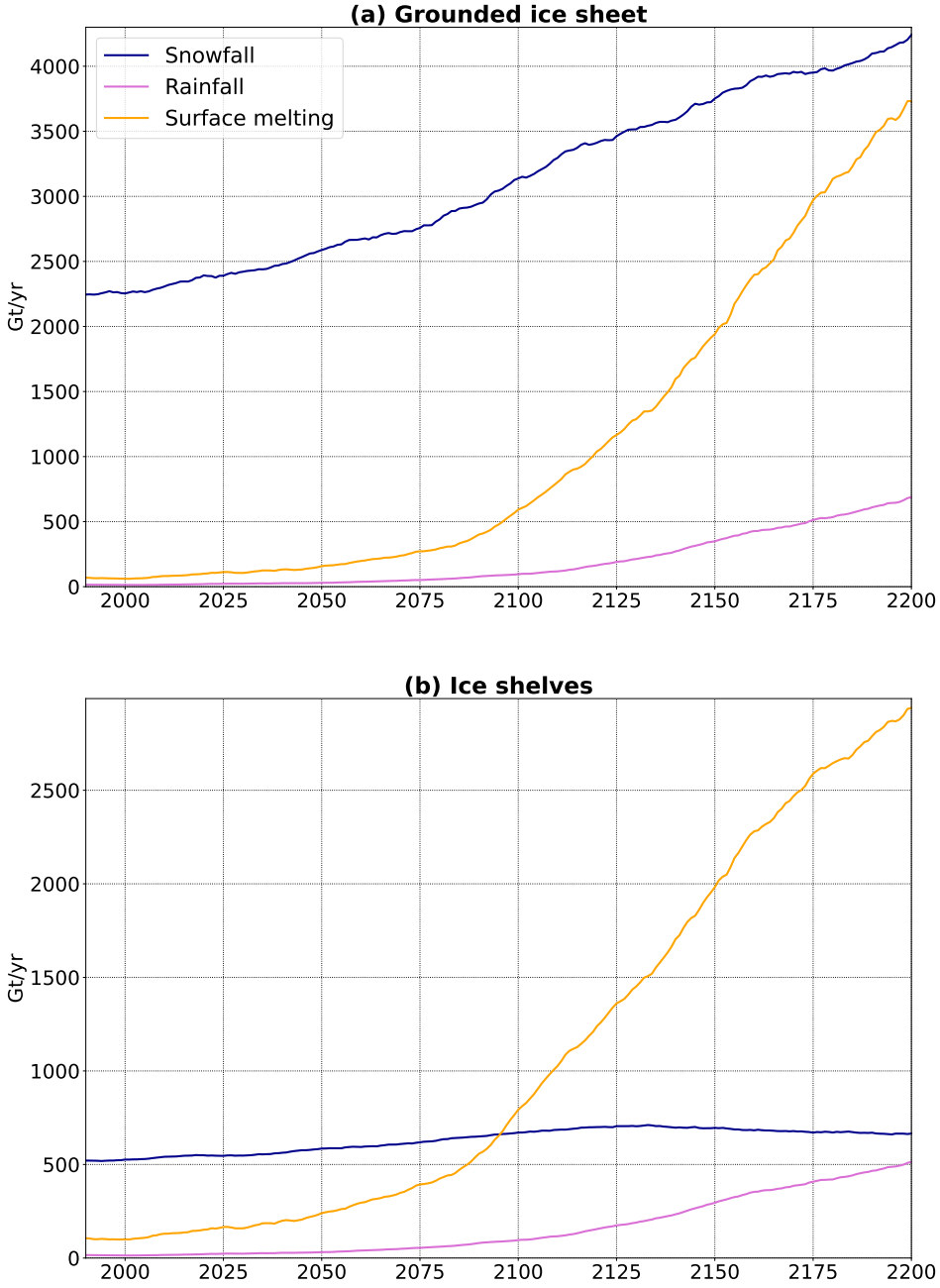

Figure B1. Total snowfall, rainfall and surface melting at the surface of (a) the grounded ice sheet and (b) the ice shelves in the MAR–IPSL-CM6A-LR–SSP5-8.5 simulation. A running average of 21 years has been used for all time series.

Here, accounting for rainfall is equivalent to having an effective threshold r of 0.52 instead of 0.64, which has a relatively small effect (see sensitivity to r in Fig. 2). A similar calculation for the ice shelves at year 2200 ($\mathrm{RF} = 0.43\,\mathrm{PR}$) gives an effective threshold r of 0.21. This means that for a given melt rate, runoff is produced more easily than predicted by our emulation method due to the decreasing proportion of solid precipitation towards year 2200. The ice-shelf surface melt rate at 2200 is nonetheless much higher than the snowfall rate (Fig. B1b), so the excess liquid water is only underestimated by 11% if we use $r = 0.64$ instead of $r = 0.21$ (from the third line of Eq. 4).

We conclude that neglecting rainfall in our emulation is a good assumption until 2100 that remains reasonable until 2200 when melting prevails.

Appendix C: Exponential fits in the parameter calibration

The a and b parameters of Eq. 4 are obtained through a least-mean-square fitting of an exponential curve for SMB minus runoff on the one hand and the surface melt rate on the other hand (Fig. C1). The fitted dataset includes the 1980–2100 period, and the 20-year reference period is 2041–2060. To remove outliers, we only consider points between the 5^{th} and the 95^{th} percentiles of the SMB minus runoff distribution, and the points where melt rate is greater than its 75^{th} percentile. The calibrated a and b parameters are listed in Tab. C1 for individual models.

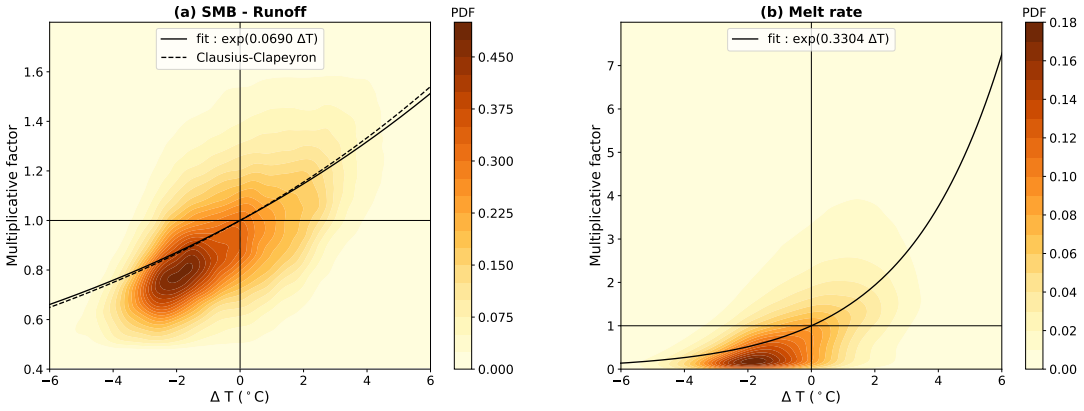

Figure C1. Factor by which the SMB minus runoff (a) and the surface melt rate (b) are multiplied versus the associated ΔT with respect to 2041–2060. This plot corresponds to MAR–IPSL-CM6A-LR. The Probability Density Function (PDF) is calculated through a Gaussian kernel density estimate, from the annual means at every grid point on the ice sheet. The dashed line in panel (a) represents the Clausius-Clapeyron exponential law.

Appendix D: Evaluation of the emulated SMB spatial patterns

Here we provide evidence that the three applications of our emulation method (Fig. 1) are able to represent the spatial SMB patterns (Fig. D1,D2,D3). For a reason that remains elusive, the largest mismatch is found on the Ross ice shelf, where the

Table C1. Fit parameters for accumulation and melt rate (see Eq. 4).

Model	a	b
MAR–IPSL-CM6A-LR	0.069	0.330
MAR–UKESM1-0-LL	0.065	0.313
MAR–CNRM-CM6-1	0.067	0.284
MAR–MPI-ESM1-2-HR	0.071	0.335
MAR–CESM2	0.065	0.303
MAR–ACCESS1-3	0.058	0.320
MAR–NorESM1-M	0.080	0.358
Mean	0.068	0.320

emulation produces a negative SMB around 2100 for the three applications, while it remains mostly positive in the original MAR simulation.

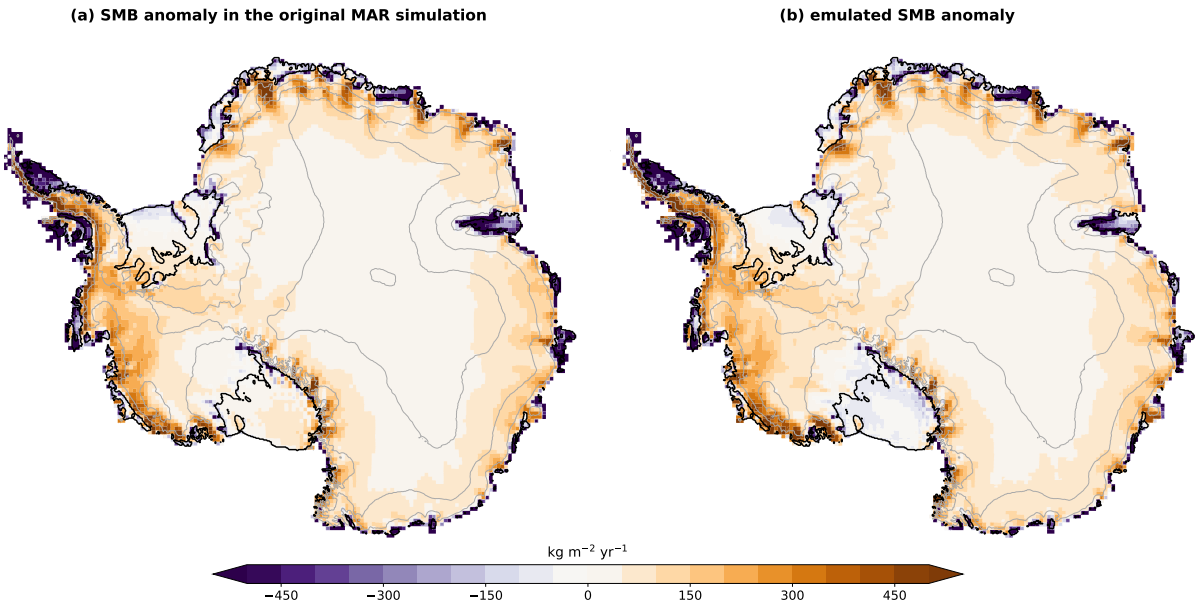

Figure D1. Evaluation of the emulation from another period (Fig. 1a). Mean SMB anomaly over 2101–2120 under the SSP5-8.5 scenario, (a) simulated by MAR–IPSL-CM6A-LR, and (b) emulated from the 2081–2100 period. The anomalies are calculated with respect to the 1995–2014 mean.

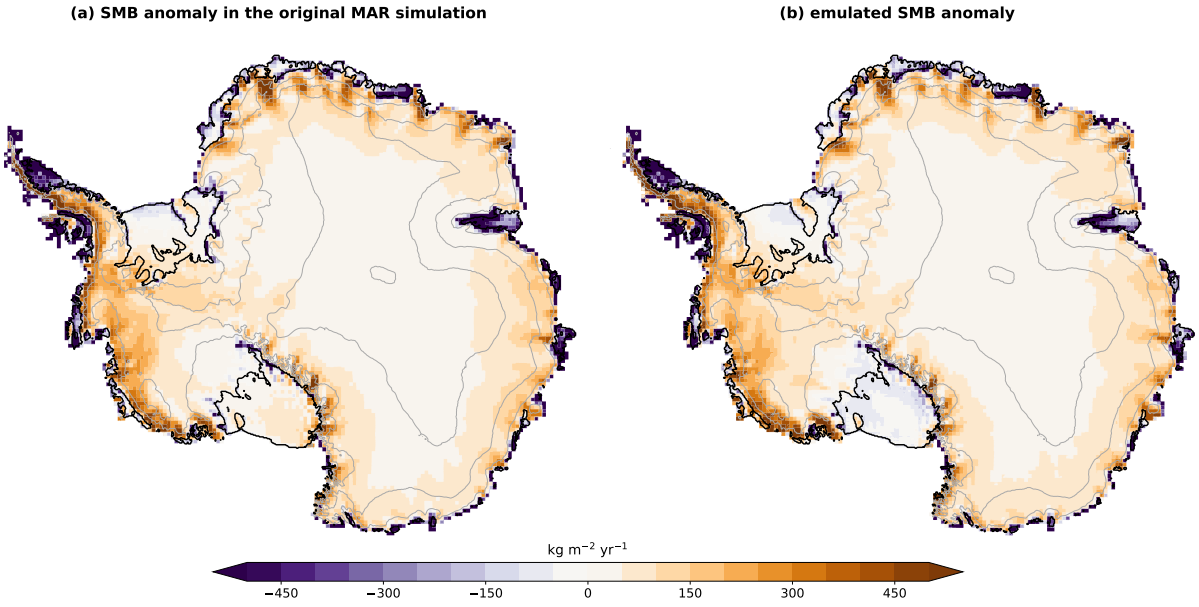

Figure D2. Evaluation of the emulation from another scenario (Fig. 1b). Mean SMB anomaly over 2081–2100 under the SSP2-4.5 scenario, (a) simulated by three MAR simulations (MAR–CESM2, MAR–UKESM1-0-LL, MAR–MPI-ESM1-2-HR), and (b) emulated from the corresponding MAR simulations under the SSP5-8.5 scenario. The anomalies are calculated with respect to the 1995–2014 mean.

Appendix E: Ice shelf surface mass balance

Here we describe the surface mass balance of ice shelves, which is relevant for the estimation of ice shelf thinning rate, which can mechanically precondition hydrofracturing. In this appendix, and only here, we assume that the ~~liquid water in excess~~ excess liquid water over the ice shelves is entirely removed as runoff, i.e., that there is no ponding. This is somewhat inconsistent with our assumptions in section 3.2 and gives SMB estimates that are slightly underestimated in warm conditions.

Our projections indicate that the SMB over ice shelves has slightly increased over the 19$^{\text{th}}$ and 20$^{\text{th}}$ centuries, and it is not expected to significantly evolve throughout the 21$^{\text{st}}$ century under SSP1-2.6 and SSP2-4.5 (Fig. E1). The SMB even increases by a few tens of $\mathrm{Gt\,yr^{-1}}$ along the 22$^{\text{nd}}$ century under SSP1-2.6 (Fig. E2).

The SSP5-8.5 SMB projections over ice shelves have a considerable spread, with a median close to present-day values and most of the weighted distribution within the historical range until 2100, but the 5$^{\text{th}}$ percentiles approaches -400 $\mathrm{Gt\,yr^{-1}}$ of anomaly by 2100 (Fig. E1). This is due to the emerging importance of ice shelf runoff at the end of the 21$^{\text{st}}$ century in the warmest simulations.

The ice shelves under SSP5-8.5 experience a net surface mass loss after 2090 to 2125 (depending on the model), with the exception of MAR–GISS-E2-1-H that stabilizes slightly above the zero SMB limit. The most extreme surface mass loss at 2200 is reached by MAR–CanESM5, which has the highest ECS of our ensemble, and is equivalent to an average ice shelf thinning rate of 2 $\mathrm{m\,yr^{-1}}$ (assuming an ice density of 920 $\mathrm{kg\,m^{-3}}$). Spatially, runoff anomalies overwhelm accumulation

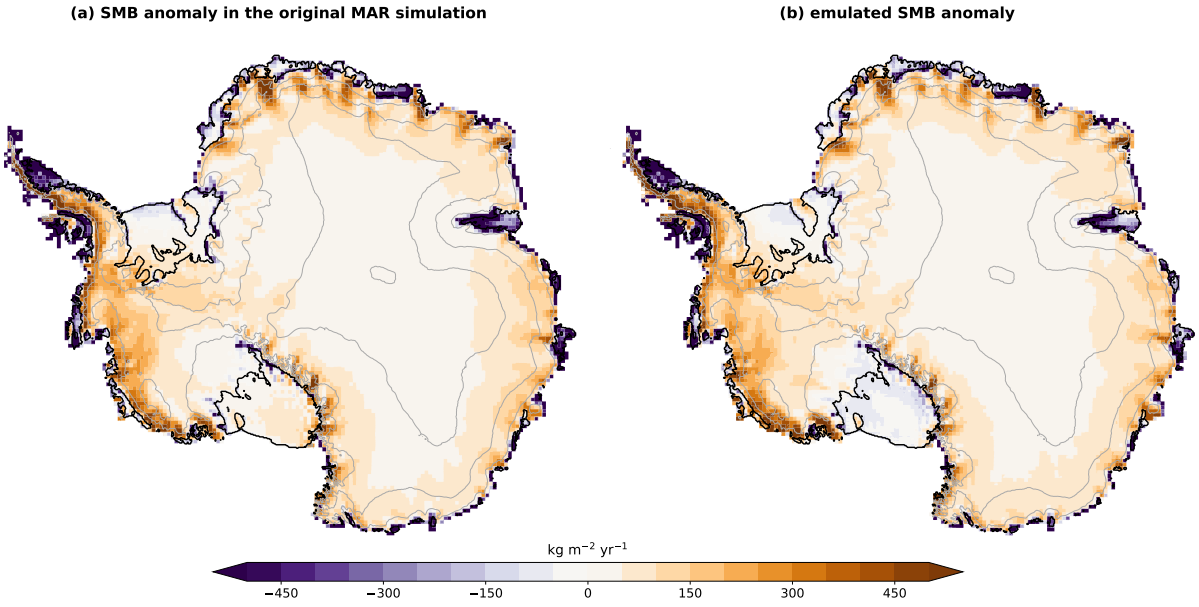

Figure D3. Evaluation of the emulation from MAR simulations driven by five other CMIP models (Fig. 1c). Mean SMB anomaly over 2081–2100 under the SSP2-4.5 scenario, (a) simulated by three MAR simulations (MAR–CESM2, MAR–UKESM1-0-LL, MAR–MPI-ESM1-2-HR), and (b) emulated for these three models, from MAR simulations driven by five other CMIP models (as in Fig. 5). The anomalies are calculated with respect to the 1995–2014 mean.

anomalies for several ice shelves of the Antarctic Peninsula before 2100 in the three scenarios (Fig. ~~??~~10), and this becomes more widespread around Antarctica after 2100 under SSP5-8.5 (Fig. ~~??~~11). In East Antarctica, runoff ~~anomaly~~ anomalies first prevail near the ice shelf grounding lines (Fig. ~~??~~10), likely due to the diabatic heating of downsloping katabatic winds and enhanced melt-albedo feedback, as previously observed by Lenaerts et al. (2017).

Author contributions. NCJ designed the overall study, developed the statistical-physical method, made the analyses and wrote the initial draft. CA and CK produced the MAR simulations. GD, CA and CK discussed the results and contributed to the manuscript.

Competing interests. Nicolas Jourdain is an editor of The Cryosphere.

Acknowledgements. This work was funded by the European Union's Horizon 2020 research and innovation programme under grant agreements No 869304 (PROTECT) and No 101003826 (CRiceS), and by the French National Research Agency under grant No ANR-22-CE01-

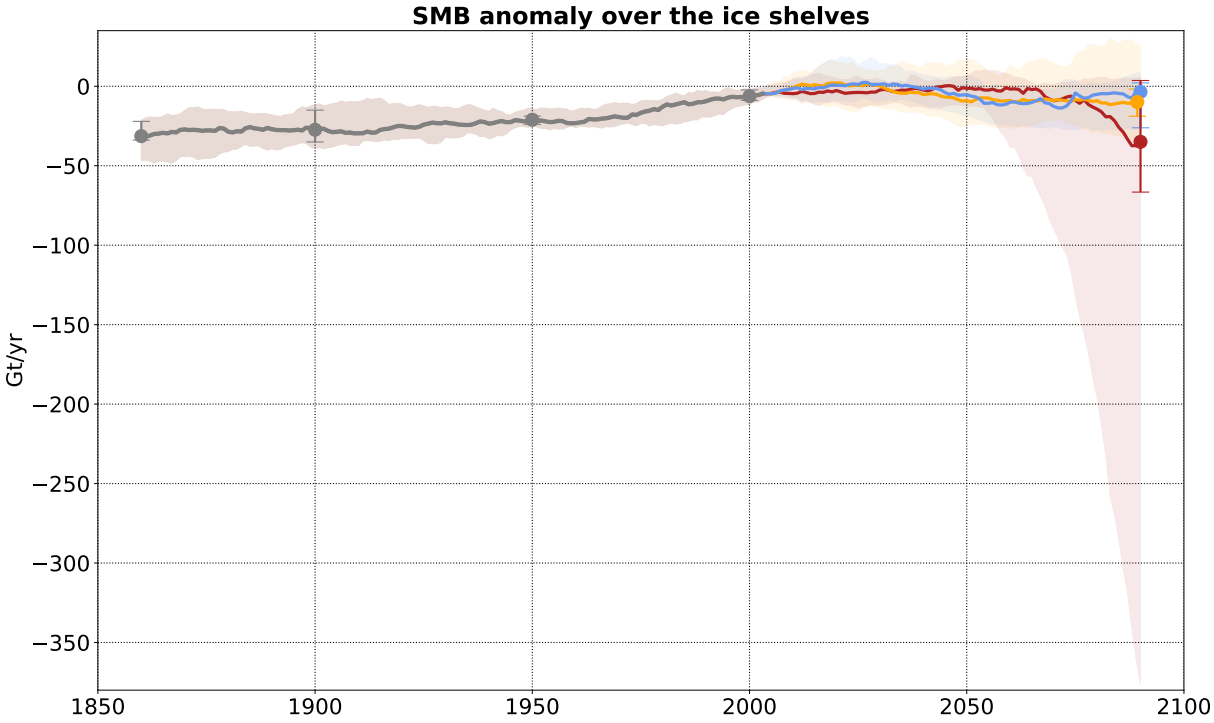

Figure E1. Emulated ensemble of surface mass balance over the Antarctic ice shelves for the historical period and three SSP scenarios. The median and percentiles are calculated based on the 16-model ensemble weighted to match with the very likely range of ECS (see section ??2.4). A 21-year running average has been used for all the time series.

0014 (AIAI). The work also benefited from the support of the French Government through the France 2030 program managed by ANR (ISClim, ANR-22-EXTR-0010). This publication is PROTECT contribution number XX.

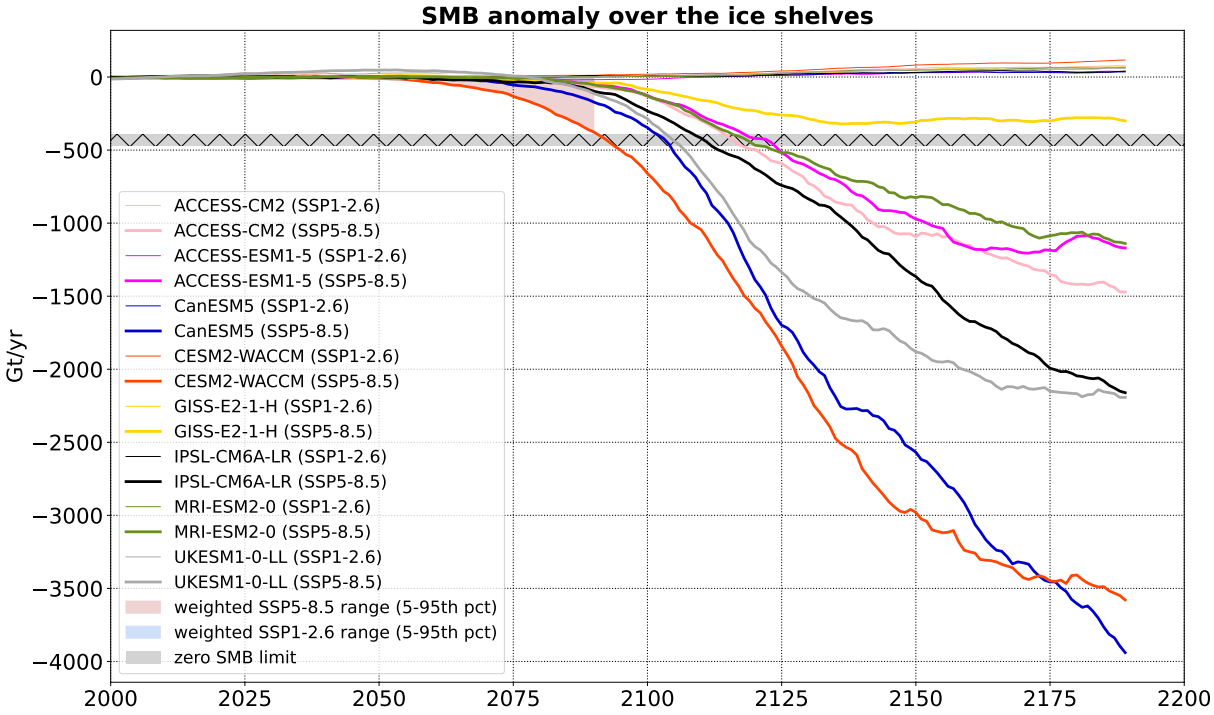

Figure E2. Eight emulations of surface mass balance over the Antarctic ice shelves for the SSP-1.26 and SSP5-8.5 scenarios. The very likely range from 16 emulations over 2000–2100 (same as Fig. E1) is also shown. The hatched area indicates the anomaly interval at which SMB reaches zero, according to the MAR, RACMO and HIRHAM present-day values reported in Mottram et al. (2021). A 21-year running average has been used for all the time series.

References

Agosta, C., Amory, C., Kittel, C., Orsi, A., Favier, V., Gallée, H., van den Broeke, M. R., Lenaerts, J., van Wessem, J. M., van de Berg, W. J., et al.: Estimation of the Antarctic surface mass balance using the regional climate model MAR (1979-2015) and identification of dominant processes, The Cryosphere, 13, 281–296, 2019.

Agosta, C., Davrinche, C., Kittel, C., Amory, C., and Edwards, T.: Evaluation of CMIP5 and CMIP6 global climate models in the Arctic and Antarctic regions, atmosphere and surface ocean, Tech. rep., Zenodo, https://doi.org/10.5281/zenodo.11595213, 2024.

Alley, K. E., Scambos, T. A., Miller, J. Z., Long, D. G., and MacFerrin, M.: Quantifying vulnerability of Antarctic ice shelves to hydrofracture using microwave scattering properties, Remote Sensing of Environment, 210, 297–306, 2018.

Arthur, J. F., Stokes, C., Jamieson, S. S. R., Carr, J. R., and Leeson, A. A.: Recent understanding of Antarctic supraglacial lakes using satellite remote sensing, Prog. Phys. Geogr. Earth Environ., 44, 837–869, 2020.

Arthur, J. F., Stokes, C. R., Jamieson, S. S. R., Carr, R. J., Leeson, A. A., and Verjans, V.: Large interannual variability in supraglacial lakes around East Antarctica, Nature Comm., 13, 1711, 2022.

Banwell, A. F., MacAyeal, D. R., and Sergienko, O. V.: Breakup of the Larsen B Ice Shelf triggered by chain reaction drainage of supraglacial lakes, Geophys. Res. Lett., 40, 5872–5876, 2013.

Banwell, A. F., Willis, I. C., Macdonald, G. J., Goodsell, B., and MacAyeal, D. R.: Direct measurements of ice-shelf flexure caused by surface meltwater ponding and drainage, Nature Comm., 10, 730, 2019.

Banwell, A. F., Datta, R. T., Dell, R. L., Moussavi, M., Brucker, L., Picard, G., Shuman, C. A., and Stevens, L. A.: The 32-year record-high surface melt in 2019/2020 on the northern George VI Ice Shelf, Antarctic Peninsula, The Cryosphere, 15, 909–925, 2021.

Barthel, A., Agosta, C., Little, C. M., Hatterman, T., Jourdain, N. C., Goelzer, H., Nowicki, S., Seroussi, H., Straneo, F., and Bracegirdle, T. J.: CMIP5 model selection for ISMIP6 ice sheet model forcing: Greenland and Antarctica, The Cryosphere, 14, 855–879, https://doi.org/10.5194/tc-14-855-2020, 2020.

Bell, R. E., Banwell, A. F., Trusel, L. D., and Kingslake, J.: Antarctic surface hydrology and impacts on ice-sheet mass balance, Nature Climate Change, 8, 1044–1052, 2018.

Bi, D., Dix, M., Marsland, S., O'farrell, S., Sullivan, A., Bodman, R., Law, R., Harman, I., Srbinovsky, J., Rashid, H. A., et al.: Configuration and spin-up of ACCESS-CM2, the new generation Australian community climate and earth system simulator coupled model, Journal of Southern Hemisphere Earth Systems Science, 70, 225–251, 2020.

Boucher, O., Servonnat, J., Albright, A. L., Aumont, O., Balkanski, Y., Bastrikov, V., Bekki, S., Bonnet, R., Bony, S., Bopp, L., et al.: Presentation and evaluation of the IPSL-CM6A-LR climate model, J. Adv. Model. Ea. Sys., 12, e2019MS002 010, 2020.

Braun, M., Humbert, A., and Moll, A.: Changes of Wilkins Ice Shelf over the past 15 years and inferences on its stability, The Cryosphere, 3, 41–56, 2009.

Caillet, J., Jourdain, N. C., Mathiot, P., Gillet-Chaulet, F., Urruty, B., Burgard, C., Amory, C., Kittel, C., and Chekki, M.: Uncertainty in the projected Antarctic contribution to sea level due to internal climate variability, EGUsphere, 2024, 1–27, 2024.

Church, J. A., Clark, P. U., Cazenave, A., Gregory, J. M., Jevrejeva, S., Levermann, A., Merrifield, M. A., Milne, G. A., Nerem, R. S., Nunn, P. D., et al.: Sea-level rise by 2100, Science, 342, 1445–1445, 2013.

Cook, A. J. and Vaughan, D. G.: Overview of areal changes of the ice shelves on the Antarctic Peninsula over the past 50 years, The cryosphere, 4, 77–98, 2010.

Costi, J., Arigony-Neto, J., Braun, M., Mavlyudov, B., Barrand, N. E., Da Silva, A. B., Marques, W. C., and Simoes, J. C.: Estimating surface melt and runoff on the Antarctic Peninsula using ERA-Interim reanalysis data, Antarctic Science, 30, 379–393, 2018.

Coulon, V., Klose, A. K., Kittel, C., Edwards, T., Turner, F., Winkelmann, R., and Pattyn, F.: Disentangling the drivers of future Antarctic ice loss with a historically-calibrated ice-sheet model, Submitted to The Cryosphere, 0, 1–42, 2023.

Danabasoglu, G., Lamarque, J.-F., Bacmeister, J., Bailey, D. A., DuVivier, A. K., Edwards, J., Emmons, L. K., Fasullo, J., Garcia, R., Gettelman, A., et al.: The community earth system model version 2 (CESM2), J. Adv. Model. Ea. Sys., 12, e2019MS001 916, 2020.

Dell, R. L., Willis, I. C., Arnold, N. S., Banwell, A. F., and de Roda Husman, S.: Substantial contribution of slush to meltwater area across Antarctic ice shelves, Nature Geosci., 17, 624–630, 2024.

Doake, C. S. M. and Vaughan, D. G.: Rapid disintegration of the Wordie Ice Shelf in response to atmospheric warming, Nature, 350, 328–330, 1991.

Donat-Magnin, M., Jourdain, N. C., Gallée, H., Amory, C., Kittel, C., Fettweis, X., Wille, J. D., Favier, V., Drira, A., and Agosta, C.: Interannual Variability of Summer Surface Mass Balance and Surface Melting in the Amundsen Sector, West Antarctica, The Cryosphere, 14, 229–249, 2020.

Donat-Magnin, M., Jourdain, N. C., Kittel, C., Agosta, C., Amory, C., Gallée, H., Krinner, G., and Chekki, M.: Future surface mass balance and surface melt in the Amundsen sector of the West Antarctic Ice Sheet, The Cryosphere, 15, 571–593, 2021.

Dunmire, D., Lenaerts, J., Datta, R. T., and Gorte, T.: Antarctic surface climate and surface mass balance in the Community Earth System Model version 2 during the satellite era and into the future (1979–2100), The Cryosphere, 16, 4163–4184, 2022.

Dunmire, D., Wever, N., Banwell, A. F., and Lenaerts, J. T. M.: Antarctic-wide ice-shelf firn emulation reveals robust future firn air depletion signal for the Antarctic Peninsula, Comm. Earth Env., 5, 100, 2024.

Dunne, J. P., Horowitz, L. W., Adcroft, A. J., Ginoux, P., Held, I. M., John, J. G., Krasting, J. P., Malyshev, S., Naik, V., Paulot, F., et al.: The GFDL Earth System Model version 4.1 (GFDL-ESM 4.1): Overall coupled model description and simulation characteristics, J. Adv. Model. Ea. Sys., 12, e2019MS002 015, 2020.

Durand, G., van den Broeke, M. R., Le Cozannet, G., Edwards, T. L., Holland, P. R., Jourdain, N. C., Marzeion, B., Mottram, R., Nicholls, R. J., Pattyn, F., et al.: Sea-level rise: From global perspectives to local services, Frontiers in Marine Science, 8, 709 595, 2022.

Edwards, T. L., Nowicki, S., Marzeion, B., Hock, R., Goelzer, H., Seroussi, H., Jourdain, N. C., Slater, D. A., Turner, F. E., Smith, C. J., et al.: Projected land ice contributions to twenty-first-century sea level rise, Nature, 593, 74–82, 2021.

Eyring, V., Bony, S., Meehl, G. A., Senior, C. A., Stevens, B., Stouffer, R. J., and Taylor, K. E.: Overview of the Coupled Model Intercomparison Project Phase 6 (CMIP6) experimental design and organization, Geosci. Model Dev., 9, 1937–1958, 2016.

Forster, P., Storelvmo, T., Armour, K., Collins, W., Dufresne, J.-L., Frame, D., Lunt, D., Mauritsen, T., Palmer, M., Watanabe, M., et al.: The Earth's energy budget, climate feedbacks, and climate sensitivity, in: Climate Change 2021: The Physical Science Basis. Contribution of Working Group I to the Sixth Assessment Report of the Intergovernmental Panel on Climate Change, pp. 923–1054, [Masson-Delmotte,V., P. Zhai,A. Pirani, S.L. Connors, C. Péan, S. Berger, N. Caud,Y. Chen, L. Goldfarb, M.I. Gomis, M. Huang, K. Leitzell, E. Lonnoy, J.B.R. Matthews, T.K. Maycock, T. Waterfield, O. Yelekçi, R. Yu, and B. Zhou (eds.)]. Cambridge University Press, Cambridge, United Kingdom and New York, NY, USA, 2021.

Fox-Kemper, B., Hewitt, H. T., Xiao, C., Aðalgeirsdóttir, G., Drijfhout, S. S., Edwards, T. L., Golledge, N. R., Hemer, M., Kopp, R. E., Krinner, G., Mix, A., Notz, D., Nowicki, S., Nurhati, I. S., Ruiz, J., Sallée, J.-B., Slangen, A. B. A., and Yu, Y.: Chapter 9: Ocean, Cryosphere and Sea Level Change, in: Climate Change 2021: The Physical Science Basis. Contribution of Working Group I to the Sixth Assessment Report of the Intergovernmental Panel on Climate Change, pp. 1211—-1362, [Masson-Delmotte,V., P. Zhai,A. Pirani, S.L. Connors, C. Péan, S. Berger, N. Caud,Y. Chen, L. Goldfarb, M.I. Gomis, M. Huang, K. Leitzell, E. Lonnoy, J.B.R. Matthews, T.K. Maycock, T. Waterfield, O. Yelekçi, R. Yu, and B. Zhou (eds.)]. Cambridge University Press, Cambridge, United Kingdom and New York, NY, USA, https://doi.org/10.1017/9781009157896.011, 2021.

Fretwell, P., Pritchard, H. D., Vaughan, D. G., Bamber, J. L., Barrand, N. E., Bell, R., Bianchi, C., Bingham, R. G., Blankenship, D. D., Casassa, G., et al.: Bedmap2: improved ice bed, surface and thickness datasets for Antarctica, The Cryosphere, 7, 2013.

Fürst, J. J., Durand, G., Gillet-Chaulet, F., Tavard, L., Rankl, M., Braun, M., and Gagliardini, O.: The safety band of Antarctic ice shelves, Nature Climate Change, 6, 479–482, 2016.

Gadde, S. and van de Berg, W. J.: Contribution of blowing-snow sublimation to the surface mass balance of Antarctica, The Cryosphere, 18, 4933–4953, 2024.

Gallée, H.: Simulation of the mesocyclonic activity in the Ross Sea, Antarctica, Monthly Wea. Rev., 123, 2051–2069, 1995.

Gallée, H. and Schayes, G.: Development of a three-dimensional meso-γ primitive equation model: katabatic winds simulation in the area of Terra Nova Bay, Antarctica, Monthly Wea. Rev., 122, 671–685, 1994.

Gettelman, A., Mills, M. J., Kinnison, D. E., Garcia, R. R., Smith, A. K., Marsh, D. R., Tilmes, S., Vitt, F., Bardeen, C. G., McInerny, J., et al.: The whole atmosphere community climate model version 6 (WACCM6), J. Geophys. Res. Atmos., 124, 12 380–12 403, 2019.

Gilbert, E. and Kittel, C.: Surface melt and runoff on Antarctic ice shelves at 1.5 C, 2 C, and 4 C of future warming, Geophys. Res. Lett., 48, e2020GL091 733, 2021.

Glaude, Q., Noël, B., Olesen, M., Van den Broeke, M., van de Berg, W. J., Mottram, R., Hansen, N., Delhasse, A., Amory, C., Kittel, C., et al.: A factor two difference in 21st-century Greenland ice sheet surface mass balance projections from three regional climate models under a strong warming scenario (SSP5-8.5), Geophys. Res. Lett., 51, e2024GL111 902, 2024.

Gorte, T., Lenaerts, J. T. M., and Medley, B.: Scoring Antarctic surface mass balance in climate models to refine future projections, The Cryosphere, 14, 4719–4733, 2020.

Greene, C. A., Gardner, A. S., Schlegel, N.-J., and Fraser, A. D.: Antarctic calving loss rivals ice-shelf thinning, Nature, 609, 948–953, 2022.

Gregory, J. M. and Huybrechts, P.: Ice-sheet contributions to future sea-level change, Philos. Trans. Royal Soc. A, 364, 1709–1732, 2006.

Hausfather, Z., Marvel, K., Schmidt, G. A., Nielsen-Gammon, J. W., and Zelinka, M.: Climate simulations: Recognize the 'hot model'problem, Nature, 605, 26–29, 2022.

Held, I. M., Guo, H., Adcroft, A., Dunne, J. P., Horowitz, L. W., Krasting, J., Shevliakova, E., Winton, M., Zhao, M., Bushuk, M., et al.: Structure and performance of GFDL's CM4. 0 climate model, J. Adv. Model. Ea. Sys., 11, 3691–3727, 2019.

Hofer, S., Lang, C., Amory, C., Kittel, C., Delhasse, A., Tedstone, A., and Fettweis, X.: Greater Greenland Ice Sheet contribution to global sea level rise in CMIP6, Nature Comm., 11, 6289, 2020.

Holland, P. R., Corr, H. F. J., Pritchard, H. D., Vaughan, D. G., Arthern, R. J., Jenkins, A., and Tedesco, M.: The air content of Larsen ice shelf, Geophys. Res. Lett., 38, 2011.

Kelley, M., Schmidt, G. A., Nazarenko, L. S., Bauer, S. E., Ruedy, R., Russell, G. L., Ackerman, A. S., Aleinov, I., Bauer, M., Bleck, R., et al.: GISS-E2. 1: Configurations and climatology, J. Adv. Model. Ea. Sys., 12, e2019MS002 025, 2020.

Kingslake, J., Ely, J. C., Das, I., and Bell, R. E.: Widespread movement of meltwater onto and across Antarctic ice shelves, Nature, 544, 349–352, 2017.

Kittel, C., Amory, C., Agosta, C., Jourdain, N. C., Hofer, S., Delhasse, A., Doutreloup, S., Huot, P.-V., Lang, C., Fichefet, T., et al.: Diverging future surface mass balance between the Antarctic ice shelves and grounded ice sheet, The Cryosphere, 15, 1215–1236, 2021.

Kittel, C., Amory, C., Hofer, S., Agosta, C., Jourdain, N. C., Gilbert, E., Le Toumelin, L., Vignon, É., Gallée, H., and Fettweis, X.: Clouds drive differences in future surface melt over the Antarctic ice shelves, The Cryosphere, 16, 2655–2669, 2022.

Kuipers Munneke, P., Ligtenberg, S. R. M., Van den Broeke, M. R., and Vaughan, D. G.: Firn air depletion as a precursor of Antarctic ice-shelf collapse, J. Glaciol., 60, 205–214, 2014.

LaBarbera, C. H. and MacAyeal, D. R.: Traveling supraglacial lakes on George VI ice shelf, Antarctica, Geophys. Res. Lett., 38, 2011.

Lai, C.-Y., Kingslake, J., Wearing, M. G., Chen, P.-C., Gentine, P., Li, H., Spergel, J. J., and van Wessem, J. M.: Vulnerability of Antarctica's ice shelves to meltwater-driven fracture, Nature, 584, 574–578, 2020.

Lenaerts, J. T. M., Lhermitte, S., Drews, R., Ligtenberg, S. R. M., Berger, S., Helm, V., Smeets, C. J. P. P., Van den Broeke, M. R., Van De Berg, W. J., Van Meijgaard, E., et al.: Meltwater produced by wind–albedo interaction stored in an East Antarctic ice shelf, Nature Climate Change, 7, 58, 2017.

Mathiot, P. and Jourdain, N. C.: Southern Ocean warming and Antarctic ice shelf melting in conditions plausible by late 23rd century in a high-end scenario, Ocean Science, 19, 1595–1615, 2023.

Meehl, G. A., Senior, C. A., Eyring, V., Flato, G., Lamarque, J.-F., Stouffer, R. J., Taylor, K. E., and Schlund, M.: Context for interpreting equilibrium climate sensitivity and transient climate response from the CMIP6 Earth system models, Science Adv., 6, eaba1981, 2020.

Meinshausen, M., Nicholls, Z. R. J., Lewis, J., Gidden, M. J., Vogel, E., Freund, M., Beyerle, U., Gessner, C., Nauels, A., Bauer, N., et al.: The shared socio-economic pathway (SSP) greenhouse gas concentrations and their extensions to 2500, Geosci. Model Dev., 13, 3571–3605, 2020.

Mosbeux, C., Durand, G., Jourdain, N., Gillet-Chaulet, F., Caillet, J., Coulon, V., Pattyn, F., Schoell, S., Klose, A. K., Winkelman, R., et al.: Assessing Antarctic Ice Sheet Dynamics and Sea Level Rise: Insights from PROTECT Model Intercomparison, Tech. rep., Copernicus Meetings, https://doi.org/10.5194/egusphere-egu24-17095, 2024.

Mostue, I. A., Hofer, S., Storelvmo, T., and Fettweis, X.: Cloud-and ice-albedo feedbacks drive greater Greenland ice sheet sensitivity to warming in CMIP6 than in CMIP5, The Cryosphere Discuss., pp. 1–23, 2023.

Mottram, R., Hansen, N., Kittel, C., van Wessem, J. M., Agosta, C., Amory, C., Boberg, F., van de Berg, W. J., Fettweis, X., Gossart, A., et al.: What is the surface mass balance of Antarctica? An intercomparison of regional climate model estimates, The Cryosphere, 15, 3751–3784, 2021.

Mouginot, J., Scheuchl, B., and Rignot, E.: MEaSUREs Antarctic Boundaries for IPY 2007-2009 from Satellite Radar, Version 2, Tech. rep., Boulder, Colorado USA. NASA National Snow and Ice Data Center Distributed Active Archive Center, https://doi.org/10.5067/AXE4121732AD, 2017.

Müller, W. A., Jungclaus, J. H., Mauritsen, T., Baehr, J., Bittner, M., Budich, R., Bunzel, F., Esch, M., Ghosh, R., Haak, H., et al.: A higher-resolution version of the max planck institute earth system model (MPI-ESM1. 2-HR), J. Adv. Model. Ea. Sys., 10, 1383–1413, 2018.

Naughten, K. A., Holland, P. R., and De Rydt, J.: Unavoidable future increase in West Antarctic ice-shelf melting over the twenty-first century, Nature Climate Change, 13, 1222–1228, 2023.

Noël, B., van Wessem, J. M., Wouters, B., Trusel, L., Lhermitte, S., and van den Broeke, M. R.: Higher Antarctic ice sheet accumulation and surface melt rates revealed at 2 km resolution, Nature Comm., 14, 7949, 2023.

Nowicki, S., Payne, A., Goelzer, H., Seroussi, H., Lipscomb, W., Abe-Ouchi, A., Agosta, C., Alexander, P., Asay-Davis, X., Barthel, A., Bracegirdle, T., Cullather, R., Felikson, D., Fettweis, X., Gregory, J., Hatterman, T., Jourdain, N., C., Kuipers Munneke, P., Larour, E., Little, C., Morlinghem, M., Nias, I., Shepherd, A., Simon, E., Slater, D., Smith, R., Straneo, F., Trusel, L., van den Broeke, M., and van de Wal, R.: Experimental protocol for sea level projections from ISMIP6 standalone ice sheet models, The Cryosphere, 14, 2331–2368, https://doi.org/10.5194/tc-14-2331-2020, 2020.

Nowicki, S. M. J., Payne, A., Larour, E., Seroussi, H., Goelzer, H., Lipscomb, W., Gregory, J., Abe-Ouchi, A., and Shepherd, A.: Ice Sheet Model Intercomparison Project (ISMIP6) contribution to CMIP6, Geosci. Model Dev., 9, 4521, 2016.

O'Neill, B. C., Kriegler, E., Riahi, K., Ebi, K. L., Hallegatte, S., Carter, T. R., Mathur, R., and Van Vuuren, D. P.: A new scenario framework for climate change research: the concept of shared socioeconomic pathways, Climatic Change, 122, 387–400, 2014.

Pfeffer, W. T., Meier, M. F., and Illangasekare, T. H.: Retention of Greenland runoff by refreezing: implications for projected future sea level change, J. Geophys. Res. Oceans, 96, 22 117–22 124, 1991.

Priya, M. G., Raghavendra, K. R., Dhanush, S., Rakshita, C., Mahesh, B., and Jefflin, A. R. D.: Monitoring of Melt Ponds and Supra-Glacial Lakes over Nivlisen Ice Shelf, East Antarctica, Using Satellite-Based Multispectral Data, in: Civil Engineering Innovations for Sustainable Communities with Net Zero Targets, pp. 297–308, CRC Press, https://doi.org/10.1201/9781032686899-24, 2024.

Rignot, E., Mouginot, J., Scheuchl, B., van den Broeke, M., van Wessem, M. J., and Morlighem, M.: Four decades of Antarctic Ice Sheet mass balance from 1979–2017, Proceedings of the National Academy of Sciences, 116, 1095–1103, 2019.

Robel, A. A. and Banwell, A. F.: A speed limit on ice shelf collapse through hydrofracture, Geophys. Res. Lett., 46, 12 092–12 100, 2019.

Rodehacke, C. B., Pfeiffer, M., Semmler, T., Gurses, Ö., and Kleiner, T.: Future sea level contribution from Antarctica inferred from CMIP5 model forcing and its dependence on precipitation ansatz, Ea. Sys. Dyn., 11, 1153–1194, 2020.

Rott, H., Skvarca, P., and Nagler, T.: Rapid collapse of northern Larsen ice shelf, Antarctica, Science, 271, 788–792, 1996.

Rott, H., Rack, W., Skvarca, P., and De Angelis, H.: Northern Larsen ice shelf, Antarctica: Further retreat after collapse, Ann. Glaciol., 34, 277–282, 2002.

Saunderson, D., Mackintosh, A., McCormack, F., Jones, R. S., and Picard, G.: Surface melt on the Shackleton Ice Shelf, East Antarctica (2003–2021), The Cryosphere, 16, 4553–4569, 2022.

Scambos, T., Hulbe, C., and Fahnestock, M.: Climate-Induced Ice Shelf Disintegration in the Antarctic Peninsula, Antarctic Peninsula Climate Variability: Historical and Paleoenvironmental Perspectives, 79, 79–92, 2003.

Scambos, T., Fricker, H. A., Liu, C.-C., Bohlander, J., Fastook, J., Sargent, A., Massom, R., and Wu, A.-M.: Ice shelf disintegration by plate bending and hydro-fracture: Satellite observations and model results of the 2008 Wilkins ice shelf break-ups, Earth Planet. Sc. Lett., 280, 51–60, 2009.

Séférian, R., Nabat, P., Michou, M., Saint-Martin, D., Voldoire, A., Colin, J., Decharme, B., Delire, C., Berthet, S., Chevallier, M., et al.: Evaluation of CNRM Earth System Model, CNRM-ESM2-1: Role of Earth system processes in present-day and future climate, J. Adv. Model. Ea. Sys., 11, 4182–4227, 2019.

Seland, Ø., Bentsen, M., Olivié, D., Toniazzo, T., Gjermundsen, A., Graff, L. S., Debernard, J. B., Gupta, A. K., He, Y.-C., Kirkevåg, A., et al.: Overview of the Norwegian Earth System Model (NorESM2) and key climate response of CMIP6 DECK, historical, and scenario simulations, Geosci. Model Dev., 13, 6165–6200, 2020.

Sellar, A. A., Walton, J., Jones, C. G., Wood, R., Abraham, N. L., Andrejczuk, M., Andrews, M. B., Andrews, T., Archibald, A. T., de Mora, L., et al.: Implementation of UK Earth system models for CMIP6, J. Adv. Model. Ea. Sys., 12, e2019MS001 946, 2020.

Sellevold, R. and Vizcaino, M.: First application of artificial neural networks to estimate 21st century Greenland ice sheet surface melt, Geophys. Res. Lett., 48, e2021GL092 449, 2021.

Sergienko, O. and Macayeal, D. R.: Surface melting on Larsen ice shelf, Antarctica, Ann. Glaciol., 40, 215–218, 2005.

Seroussi, H., Nowicki, S., Payne, A. J., Goelzer, H., Lipscomb, W. H., Abe-Ouchi, A., Agosta, C., Albrecht, T., Asay-Davis, X., Barthel, A., et al.: ISMIP6 Antarctica: a multi-model ensemble of the Antarctic ice sheet evolution over the 21st century, The Cryosphere, 14, 3033–3070, 2020.

Seroussi, H., Pelle, T., Lipscomb, W. H., Abe-Ouchi, A., Albrecht, T., Alvarez-Solas, J., Asay-Davis, X., Barre, J.-B., Berends, C. J., Bernales, J., et al.: Evolution of the Antarctic Ice Sheet over the next three centuries from an ISMIP6 model ensemble, Earth's Future, 12, e2024EF004 561, 2024.

Shepherd, A., Wingham, D., Payne, T., and Skvarca, P.: Larsen ice shelf has progressively thinned, Science, 302, 856–859, 2003.

Skvarca, P., De Angelis, H., and Zakrajsek, A. F.: Climatic conditions, mass balance and dynamics of Larsen B ice shelf, Antarctic Peninsula, prior to collapse, Ann. Glaciol., 39, 557–562, 2004.

Spergel, J. J., Kingslake, J., Creyts, T., van Wessem, M., and Fricker, H. A.: Surface meltwater drainage and ponding on Amery Ice Shelf, East Antarctica, 1973–2019, J. Glaciol., 67, 985–998, 2021.

Stokes, C. R., Sanderson, J. E., Miles, B. W. J., Jamieson, S. S. R., and Leeson, A. A.: Widespread distribution of supraglacial lakes around the margin of the East Antarctic Ice Sheet, Sci. Rep., 9, 13 823, 2019.

Sun, S., Pattyn, F., Simon, E. G., Albrecht, T., Cornford, S., Calov, R., Dumas, C., Gillet-Chaulet, F., Goelzer, H., Golledge, N. R., et al.: Antarctic ice sheet response to sudden and sustained ice-shelf collapse (ABUMIP), J. Glaciol., 66, 891–904, 2020.

Swart, N. C., Cole, J. N. S., Kharin, V. V., Lazare, M., Scinocca, J. F., Gillett, N. P., Anstey, J., Arora, V., Christian, J. R., Hanna, S., et al.: The Canadian earth system model version 5 (CanESM5. 0.3), Geosci. Mod. Dev., 12, 4823–4873, 2019.

Thomas, E. R., Van Wessem, J. M., Roberts, J., Isaksson, E., Schlosser, E., Fudge, T. J., Vallelonga, P., Medley, B., Lenaerts, J., Bertler, N., et al.: Regional Antarctic snow accumulation over the past 1000 years, Climate of the Past, 13, 1491–1513, 2017.

Trusel, L. D., Frey, K. E., Das, S. B., Karnauskas, K. B., Kuipers Munneke, P., van Meijgaard, E., and van den Broeke, M. R.: Divergent trajectories of Antarctic surface melt under two twenty-first-century climate scenarios, Nature Geoscience, 8, 927–932, 2015.

Tsai, C.-Y., Forest, C. E., and Pollard, D.: The role of internal climate variability in projecting Antarctica's contribution to future sea-level rise, Clim. Dynam., 55, 1875–1892, 2020.

van den Broeke, M.: Strong surface melting preceded collapse of Antarctic Peninsula ice shelf, Geophys. Res. Lett., 32, L12 815, https://doi.org/10.1029/2005GL023247, 2005.

van der Meer, M., de Roda Husman, S., and Lhermitte, S.: Deep learning regional climate model emulators: A comparison of two downscaling training frameworks, J. Adv. Model. Earth Sys., 15, e2022MS003 593, 2023.

van Wessem, J. M., Ligtenberg, S. R. M., Reijmer, C. H., van de Berg, W. J., van den Broeke, M. R., Barrand, N. E., Thomas, E. R., Turner, J., Wuite, J., Scambos, T. A., and van Meijgaard, E.: The modelled surface mass balance of the Antarctic Peninsula at 5.5 km horizontal resolution, The Cryosphere, 10, 271–285, 2016.

van Wessem, J. M., van den Broeke, M. R., Wouters, B., and Lhermitte, S.: Variable temperature thresholds of melt pond formation on Antarctic ice shelves, Nature Climate Change, 13, 161–166, 2023.

Veldhuijsen, S. B. M., Van De Berg, W. J., Kuipers Munneke, P., and Van Den Broeke, M. R.: Firn air content changes on Antarctic ice shelves under three future warming scenarios, The Cryosphere, 18, 1983–1999, 2024.

Virtanen, P., Gommers, R., Oliphant, T. E., Haberland, M., Reddy, T., Cournapeau, D., Burovski, E., Peterson, P., Weckesser, W., Bright, J., et al.: SciPy 1.0: fundamental algorithms for scientific computing in Python, Nature Methods, 17, 261–272, 2020.

Voldoire, A., Saint-Martin, D., Sénési, S., Decharme, B., Alias, A., Chevallier, M., Colin, J., Guérémy, J.-F., Michou, M., Moine, M.-P., et al.: Evaluation of CMIP6 deck experiments with CNRM-CM6-1, J. Adv. Model. Ea. Sys., 11, 2177–2213, 2019.

Volodin, E. M., Mortikov, E. V., Kostrykin, S. V., Galin, V. Y., Lykossov, V. N., Gritsun, A. S., Diansky, N. A., Gusev, A. V., and Iakovlev, N. G.: Simulation of the present-day climate with the climate model INMCM5, Clim. Dynam., 49, 3715–3734, 2017.

Wager, A. C.: Flooding of the ice shelf in George VI Sound, British Antarctic Survey Bulletin, 28, 71–74, https://nora.nerc.ac.uk/id/eprint/526223/1/bulletin28_07.pdf, 1972.

Weertman, J.: Can a water-filled crevasse reach the bottom surface of a glacier, in: Symposium on the Hydrology of Glaciers: Cambridge, 7–13 September 1969. (International Association of Scientific Hydrology), 95, pp. 139–145, 1973.

Wille, J. D., Favier, V., Jourdain, N. C., Kittel, C., Turton, J. V., Agosta, C., Gorodetskaya, I. V., Picard, G., Codron, F., Santos, C. L.-D., et al.: Intense atmospheric rivers can weaken ice shelf stability at the Antarctic Peninsula, Comm. Ea. Env., 3, 90, 2022.

Yukimoto, S., Kawai, H., Koshiro, T., Oshima, N., Yoshida, K., Urakawa, S., Tsujino, H., Deushi, M., Tanaka, T., Hosaka, M., et al.: The Meteorological Research Institute Earth System Model version 2.0, MRI-ESM2. 0: Description and basic evaluation of the physical component, Journal of the Meteorological Society of Japan. Ser. II, 97, 931–965, 2019.

Zheng, Y., Golledge, N. R., Gossart, A., Picard, G., and Leduc-Leballeur, M.: Statistically parameterizing and evaluating a positive degree-day model to estimate surface melt in Antarctica from 1979 to 2022, The Cryosphere, 17, 3667–3694, 2023.

Ziehn, T., Chamberlain, M. A., Law, R. M., Lenton, A., Bodman, R. W., Dix, M., Stevens, L., Wang, Y.-P., and Srbinovsky, J.: The Australian earth system model: ACCESS-ESM1. 5, Journal of Southern Hemisphere Earth Systems Science, 70, 193–214, 2020.